Government of **Western Australia**
Department of **Mines and Petroleum**

RECORD 2009/14

COMPLEX STRAIN IN MYLONITES FROM THE WESTERN MUSGRAVES, NORTH OF THE MANN FAULT, WESTERN AUSTRALIA

by
Althea Walker-Hallam

TRaX
Tectonics, Resources and Exploration

THE UNIVERSITY OF ADELAIDE
AUSTRALIA
SUB CRUCE LUMEN


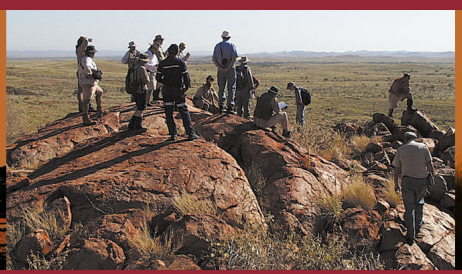

Geological Survey of
Western Australia

NGAANYATJARRA COUNCIL (Aboriginal Corporation)

Complex strain in mylonites from the Western Musgraves, North of the Mann Fault, Western Australia

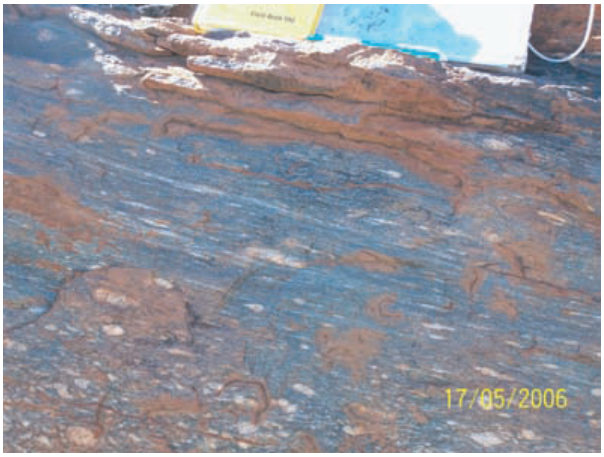

Althea Walker-Hallam
Continental Evolution Research Group
School of Earth and Environmental Sciences
University of Adelaide, South Australia

Supervisors: Dr Alan Collins
Dr David Kelsey

Date 25th of October

Notice to the reader

This Record is one of a series of BSc. Hons theses researched, written and compiled by students from the Centre of Tectonics, Resources and Exploration (TRaX), University of Adelaide, through an ongoing collaborative project between the Geological Survey of Western Australia (GSWA) and the University of Adelaide. Although GSWA has provided field and laboratory support for this project, the scientific content of each Record, and the drafting of figures, has been the responsibility of the authors. No editing has been undertaken by GSWA.

All work carried out in the west Musgrave region is done so within the framework of an ongoing collaborative project involving GSWA, the Traditional Owners of the region and the Ngaanyatjarra Council. The considerable efforts of the Traditional Owners and of the Ngaanyatjarra Council in facilitating this work is gratefully acknowledged.

Table of Contents

Complex strain in mylonites from the Western Musgraves, North of the Mann Fault, Western Australia

Althea Walker-Hallam*

Continental Evolution Research Group

School of Earth and Environmental Sciences,

Adelaide University, South Australia.

Abstract:

The Petermann Orogeny is an extensive Neoptroterozoic/Cambrian orogen that occurs in the Musgraves Province of South Australia, the Northern Territory and Western Australia. Despite its extent and unusual intracontinental origin, its timing, kinematic and metamorphic evolution are still poorly known. Spaghetti Hill is a prominent outcrop in the Western Musgrave Block that lies in the core of the Petermann Orogen and is deformed by shear zones of Petermann age. Zircon and titanite from these shear zones yielded Sensitive High Resolution Ion Microprobe (SHRIMP) protolith crystallisation $^{207}Pb/^{206}Pb$ ages of 1137±13 and 1121±11Ma, and deformation/metamorphic $^{206}Pb/^{238}U$ ages of 570±25Ma and 522±14Ma. Thermobarometric calculations using THERMOCALC indicates the deformation reached peak conditions of ~700ºC and 11kbars. Microstructural analysis using electron backscatter diffraction (EBSD) demonstrates that quartz developed a pronounced crystallographic preferred orientation (CPO) during this deformation, whilst feldspar was deformed by grain-boundary sliding. These microstructural results supported the structural mapping that demonstrated that the deformation on Spaghetti Hill was south directed despite the proximity to the inferred major, north-directed Woodroofe Thrust.

*Email: althea.walker@student.adelaide.edu.au

Keywords: Musgrave Block, Petermann Orogeny, EBSD, Structural Geology, SHRIMP, Thermobarometry.

1.Introduction

The Petermann Orogeny is a poorly dated and kinematically understood intracratonic orogen that occurs throughout the Musgraves Province of WA, SA and the NT. In the Western

Musgrave Block of WA, previous work has focused on the ~1080 Ma Giles Complex due to its prospectivity for platinum group elements minerals, detailed study of the extensive deformation caused by the Petermann Orogeny is largely restricted to the Northern Territory (Edgoose et al., 2004). The Western Musgraves are currently being mapped by Geological Survey of Western Australia (GSWA) on a 1:250,000 scale. This project was logistically supported by the GSWA and uses structural mapping, microstructure using electron backscatter diffraction (EBSD), thermobarometry and Sensitive High Resolution Ion Microprobe (SHRIMP) U-Pb dating of zircon and titanite to attempt to characterise the kinematic evolution of a part of the Western Musgraves during the Petermann Orogeny, obtain better constraints on the timing of deformation and investigate the thermobarometric conditions during deformation.

2.Regional geological setting

The Musgrave Block (Fig. 1) is located at the meeting point of the South Australian, Western Australian and Northern Territory borders. It spans around 120,000 km^2, and trends east-west. To the north of the Musgraves lies the Amadeus basin, to the east, the Eromanga basin, to the south and southwest lies the Officer basin, and to the northwest, the Canning Basin.

The oldest known rocks in the Musgrave Block are igneous and some sedimentary gneisses as old as 1550 and 1330Ma (Kelly et al., 2006). At around 1190Ma, voluminous granitic magmatism saw the emplacement of the Pitjantjatjara Supersuite (Edgoose et al., 2004), then the mafic Giles Complex intruded around 1060Ma, with volcanic equivalents in the Western Musgraves known as the Tollu Volcanics. Mafic dyke swarms have been dated at ~1000Ma and again at 800Ma (Glickson et al., 1996).

The Musgrave Block as described by White et al. (1999), among others, has undergone six phases of deformation (D1-D6). D1 at c.1300Ma and D2 at c.1200Ma produced S1 and S2 migmatitic layering. The conditions during D1 are unclear, but estimated as high temperature due to the presence of leucocratic melting (White et al., 1999). Evidence for this event is only seen in the southwest of the Musgraves (Edgoose et al., 2004). D2, known as the Musgravian Orogeny, is more widespread: White et al. (1999) reported metamorphic conditions of 800-

850ºC. and 5-6kbars in the Western Musgraves, and Camacho and Fanning, (1995) reported 660-850ºC, and 5.2-6.2kbars at Kulgera in the Eastern Musgraves.

This metamorphism was accompanied by syn-post deformational voluminous felsic magmatism (The Pitjantjatjara Supersuite, Edgoose et al., 2004). The variable pressure-temperature results are attributed to non-uniform exhumation of the Orogen, although metamorphic facies gradients or exhumation patterns cannot be constructed due to the lack of data.

Pitjantjatjara Supersuite Granite is the name proposed for related granitic intrusions that were emplaced from 1190-1120Ma (Edgoose et al., 2004). This includes units from throughout the Musgraves, but they are more abundant in the west. Intrusion accompanied regression from peak metamorphic conditions after the Musgravian Orogeny. This is found throughout the Musgraves. It ranges from megacrystic granites, exhibiting rapakivi textures, to more equigranular intrusions. From data collected in the Northern Territory, Edgoose et al. (2004) report that the primary mineral assemblage is K-feldspar rich, with plagioclase, clinopyroxene, hornblende, biotite, Fe-Ti oxides and titanite.

This granite often possesses a weak fabric, and major structures associated with the Petermann Orogeny, such as the Mann fault, cut across it. Where this produces a mylonitic fabric, the clinopyroxene can be replaced by hornblende. Garnet or epidote is often present, depending on the grade, with garnet restricted, in the Western Musgraves to north of the Mann Fault.

At 1060Ma, there was synchronous deformation (D3) with the intrusion of the Giles Complex, which caused F3 folding and is described as intensely strain partitioned (Clarke et al., 1995).
D4-D6 formed widespread mylonitic fabrics across the Musgraves. D4 caused southeast-transported ultramylonite; D5 was characterised by southwest-transported mylonite and ultramylonite, and D6, (which is synonymous with the Petermann Orogeny), is characterised by ultramylonite with pseudotachylite. The duration of this event is commonly reported at c.560-520Ma (eg Kelly et al., 2006) It was during the Petermann Orogeny that a series of large-scale,

east-west striking fault structures formed throughout the Musgrave Block and exhumed crust from up to 10km depth (Kelly et al., 2006). These structures include the Mann-Hinckley Fault, and the Woodroofe Thrust and the Champs De Mars fault which are commonly described as being north-directed (Stewart, 1995; Kelly et al., 2006). The Petermann Orogeny was a high-grade event with conditions estimated at 12-13kbar and 700-750ºC in the Northern Territory (Scrimgeour and Close, 1999), although age constraints and P-T calculations are extremely limited.

3.Structural Geology and Field Relationships

Spaghetti Hill (Fig. 2) is a horseshoe-shaped outcrop of Pitjantjatjara Supersuite granite. Mylonite zones occupy the western and southeastern edges of the hill. On the southeast side, one main shear zone extends from the south centre of the hill to the northeast corner, with some small associated shear zones branching off. They trend southwest, and dip between 20º and 40º towards the northwest. On this side of the hill, the shear zones are only a few metres in width, but widen to a plateau of around 30 metres at the south end. The rocks possess a lineation that trends almost along strike and dips shallowly southwards at the north end, and northwards at the south end. The narrow shear zone displays a fine-grained mylonitic fabric with rotated garnet porphyroblasts. Kinematic indicators, principally δ and σ clasts, which are characteristically rotated porphyroclasts, show top-to the south movement. A semi-parallel shear zone with large rotated feldspar porphyroblasts (Fig. 3) wraps around the base of the hill, but the extent of its width is concealed as it continues beneath sandy cover.

The west side of the hill is characterized by a gently sloping rise terminating in a plateau at the base of a steep ridge. The mylonite on this side of the hill is more structurally complex. The entirety of the hillside is covered in anastomosing shear zones of varying width that merge with each other and also incorporate large pods of unmylonitised granite. A narrow shear zone no more than 5 metres wide trends north-northeast along the top of the ridge, and a much wider one splits from the upper shear zone at the south corner and runs parallel to it at the base of the ridge, widening to the north. On the gentler slope below the ridge, the mylonitic fabric trends east-northeast, toward the higher shear zones. Lineation on the west side of the hill trends

uniformly northeast, and plunges between 20º and 40º to the north. A smaller scale map has been made of the central west area, known as Spaghetti Junction (see inset to Fig. 2). In this area, shear zones trend into the hill; in two places they wrap around undeformed granite pods. Cross-cutting relationships were not observed in the outcrop, however, where they meet the shear zone running north across the hill, there is often an L-tectonite between the two shear zones, and these shear zone relationships are also observed to the north of Spaghetti Junction although the outcrop was not so continuous.

At the North end of Spaghetti Junction there is complex mesoscale folding, a feature not witnessed on any other part of the hill (see Fig. 4). This may be an instance of a shear zone running parallel to those in Spaghetti Junction truncating one running parallel with those above on the ridge, however, the outcrop was not sufficiently continuous to demonstrate this conclusively.

Shear zones were mylonitised to varying degrees throughout the mapping area. The inset map of Spaghetti Junction describes the degree of mylonitisation in the area: mylonite is shown in pale blue, protomylonite is shown in dark blue, and L-tectonite, where the two groups of shear zones converge, in teal.

Shear zones on the southern and south-eastern faces of the hill are very fine grained mylonites, while mylonites on the western side were coarser, with a bluish appearance in outcrop, and highly visible stretched feldspar grains.

4. Lithological descriptions

Spaghetti Hill is comprised of two types of granite. They are either megacrystic, pink-coloured, granite with K feldspars up to 10cm in size, or a relatively equigranular greyish colour with feldspars up to 4cm. The Spaghetti Hill granite is garnet bearing, and has rare, narrow (up to about 8cm wide) felsic dykes that cut across the granite in a few places. Along the western side of the hill, and around the south and southeast edges in discrete bands, the granite has been mylonitised.

The mineralogy of the mylonite across Spaghetti Hill was relatively uniform. It contains a matrix dominated by plagioclase and quartz, with garnet, hornblende, titanite, biotite, and accessory ilmenite, iron oxides, pyrite and apatite. All samples contained abundant, large (up to 500 μm) zircons. Quartz ribbons, aligned biotite and fine-grained feldspar in many places separate the fabric into more felsic and more mafic domains. Garnets are present as porphyroblasts, up to 1cm in width in the coarsest samples (155716 and 155717); as fragmented parts of larger grains in most, and as rotated δ-type structures in the finest-grained samples (155718 and 155727 see Fig. 5). K-feldspar is present in small amounts in the matrix, but more often as large porphyroblasts up to 1cm. Some of them display perthitic texture. Hornblende is present as the remnant of large porphyroblasts; in the finest grained samples, hornblende is distributed evenly throughout the matrix as very fine grains. Titanite is present in almost all samples, and occurs as inclusions in larger grains, as fragments, or, in the finer grained samples as oval shaped grains, usually with a preferred orientation. In the finest grained samples, rounded titanite has iron oxide tails.

All the thin sections studied were of mylonitised granite. Mylonite samples were taken from a wide range of locations over the hill, and five samples were taken from a transect across a small shear zone, and exhibit a range of grain size and mylonitisation.

Transect

The transect shear zone (Fig. 6) is located on a ridge on the western side of the hill. It is approximately 17m wide, and is bounded by apparently undeformed granite with round, square or oval-shaped feldspar crystals up to 5cm in length. The deformation in the shear zone is asymmetric across the shear zone, with a region of coarse fabric (protomylonite) up to 14m wide from the western edge, and only about half a metre on the east. A finer grained area “mylonite” between them is about 1.5m wide, and an intermediate zone between them. Figure 7 shows the change in feldspar shape measured at three intervals into the centre of the shear zone from roughly euhedral in the undeformed granite, to extremely thin and elongate in the centre of the shear zone.

Despite the difference in width, the protomylonite zones (samples 155730 and 155733, Fig. 8 d) on either side have a similar fabric. Garnet occurs as small residual fragments in clusters. The fabric has different domains defined by the grains size and mineralogy. Large K-feldspar porphyroclasts occur up to one centimetre in diameter, some of which have a slightly perthitic texture occur. Large feldspar typically exhibits core-and-mantle structure, as tiny polygonal grains surround it. Smaller plagioclase, K-feldspar and quartz grains occur in ribbons. Biotite grains, up to 2mm long are aligned and concentrated with hornblende and opaque minerals. Biotite is pale yellow grey in thin section, and hornblende is pale grey green or deep bottle green, usually in the larger grains. Hornblende grains are up to 3mm in diameter, fragmented and strung out in alignment with the fabric.

In the intermediate (Fig. 8b) area between the protomylonite and the centre of the shear zone, the quartz and feldspar form bands in which equant grains are surrounded by small recrystallised grains. Within these domains there are also continuous quartz ribbons, which can be traced through the length of the thin section. Again, aligned biotite, and irregular grains of titanite and amphibole are concentrated between these domains. The amphibole is either a deep forest green, or a yellow green. Opaque minerals are present as irregular, elongate grains. Zircon is more common in the vicinity of the biotite than the quartz and feldspar, and garnet is still present as rare, small fragments.

Towards the centre (Fig. 8c) of the shear zone, the grainsize is dramatically smaller (millimetre-scale to smaller than visible with the naked eye). The fabric is dominated by biotite, which is more evenly distributed rather than concentrated in bands. There are ~2.5mm hornblende porphyroblasts, occasionally rounded but more often elongate. Here, hornblende is dark red brown or deep forest green. No garnet is present in this sample (155731), but occurs as porphyroblasts in other garnets along strike, as well as throughout the less-deformed areas of the shear zone. Quartz still forms ribbons throughout the thin section.

5.Electron Backscatter Diffraction, (EBSD)

Electron backscatter diffraction (EBSD) is a method of studying the microstructure of rocks at a lattice scale. Most simply, it determines the crystallographic orientation of a mineral and therefore can be used to identify preferred orientations of many minerals in a thin section. This in turn provides information about the kinematics, and to some extent the degree of deformation, and the temperature range at which the deformation occurred as different mechanisms and slip systems operate at different temperatures and strain rates. It can also furnish us with information about the deformation mechanisms produced, the slip systems that were active, and the variation in behaviour of different minerals. At present, the technique is still quite new and details of slip systems and temperature constraints are not available for all geological minerals. (Prior et al., 1999).

Slides of the three finest-grained samples were chosen for EBSD, on the assumption that the smallest grainsize may represent a higher intensity of deformation. They were polished with colloidal silica, and the areas selected for analysis were surrounded with carbon dag to reduce charging problems. Later samples were also given an additional ~1.3 micron carbon coat. Automated beam maps were produced with a Philips XL30 FESEM at Adelaide Microscopy, using a spot size of 4 and 15kV. The results processed using HKL Channel 5 software. In each sample, small areas high in quartz and feldspar were chosen, but the sample was indexed for the minerals quartz, anorthite, K feldspar, albite, pyrope, and amphibole, titanite. Indexing was rejected if the mean angular deviation (MAD) was greater than two. Data noise was reduced by using a Wildspike correction, and by extrapolation from four nearest neighbours, repeated several times. Zero solutions are likely to include biotite, which was omitted as the polishing process is often unsuccessful on micas (Prior et al., 1999), and titanite, which has not been indexed successfully.

Sample 155727

155727 is a very fine-grained mylonitised granite (0486753N, 7146135E UTM 52J). The matrix is made up of quartz, feldspar, and amphibole, which form compositional layers. Porphyroblasts

of titanite, feldspar and rotated garnet also occur. Optical microscopy indicates top-to-the-south kinematics based on winged porphyroblasts. This is consistent with field observations.

Phases

EBSD analysis of 155727 indicates quartz is the most abundant mineral. Figure 9a shows phases and grain boundaries superimposed on a band contrast image. Quartz is shown in green, anorthite in aqua, albite in blue, orthoclase in teal, and pyrope in purple. Within the sample's prominent foliation, quartz forms ribbons or elongate aggregates of small grains. In the upper left of the image, the grains are elongate, while in the lower right they are smaller and less elongate. Anorthite is the next most prevalent mineral, and while it is possible that this truly represents the relative amounts of albite, anorthite and orthoclase, the extremely low levels of other feldspars could be an artefact of the indexing process, whereby the software is unable to correctly identify the very similar feldspar diffraction patterns and chooses one arbitrarily. This is also supported by the higher levels of albite and orthoclase indexed in the following two samples. Use of EBSD in geosciences is comparatively new, and some minerals such as albite and FeTi oxides are not well characterised (Prior et al., 1999). Given these considerations, and the relative proportion of anorthite in this sample, feldspar is treated collectively where possible in this and the following samples. Zero solutions in this include biotite, and amphibole and titanite, which have not been indexed successfully.

Grain boundaries

A grain boundary map that is superimposed on the phase map shows the occurrence of low angle (subgrain) boundaries (<2 degrees, shown in red), and grain boundaries (<10 degrees, shown in black). Quartz shows strong development of both low and high angle boundaries. The quartz also shows Dauphinè twinning in quartz, (thick yellow line) which is undetectable under the optical microscope; these coincide with the higher angle boundaries, but are attributed to crystal growth (Neumann, 2000), or low-grade deformation. It is possible they represent late stage deformation. Feldspar also shows some development of high angle and some low angle boundaries.

All-Euler map

Figures 9b and c are of all Euler angles for quartz and feldspar. Similar colours indicate similar crystallographic orientations. They indicate two domains of quartz grains, one with elongate grains shown in pale greens and blues, and uniform orientations; the other, more euhedral grains and more random orientation, although still with a visible proportion of the same greens and blues. These domains are flanked by a domain consisting mostly of feldspar, likewise more euhedral and randomly oriented.

Misorientation histogram

Figures 10a and b are histograms of the misorientation distribution in the sample. Misorientation is expressed as the smallest rotation and angle required to bring two crystals into the same orientation (Wheeler et al., 2001). The black line is the theoretical random distribution; uncorrelated misorientation (red) is the difference in orientation of randomly distributed crystal pairs from a phase. Correlated misorientation (black) is the difference in orientation between neighbouring pairs. Ideally, misorientation angles from an undeformed rock will coincide with the theoretical random, but with increasing deformation, they will diverge from the theoretical curve, and differences in the correlated and uncorrelated misorientations imply relationships from deformation or inheritance between neighbouring grains (Wheeler et al., 2001).

The misorientation histogram of quartz in sample 155727 shows a strong deviation between the theoretical random and the correlated and uncorrelated misorientation distributions. The peak at 60º is caused by Dauphinè twinning. This distribution is consistent with the Euler map of quartz, indicating a crystallographic preferred orientation, and a relationship with nearby grains. The feldspar misorientation closely matches the theoretical random distribution.

Pole plots

Pole plots are oriented with respect to the sample such that X0 is parallel to the mineral lineation and lies in the foliation (the length of the slide), Z0 is perpendicular to the foliation and Y0 is also parallel to the foliation but is perpendicular to X0 and Z0 and comes directly out of

the slide. X_0 is interpreted as the long axis of the strain ellipse; Y_0 is the intermediate axis and Z_0 the short axis (the shortening direction).

A plot of the quartz axes indicates a strong crystallographic preferred orientation (CPO) (Fig. 11a). The c axis <0001> shows a broad maximum at a high angle to the foliation in the direction of the intermediate stress direction, and the a axis <10-10> distributed radially about the edge of the stereonet, and therefore at all angles to the foliation.

Without any other information, this quartz fabric could resemble pure shear in high-grade metamorphic rocks or simple shear at medium temperatures (Twiss and Moores, 1997) as in either deformation the c axis rotates into the intermediate stress direction. (Passchier and Trouw, 1996); however, this sample contains abundant evidence of simple shear (eg see Fig. 5), and so the fabric is interpreted as representing non-coaxial strain. Pole plots of <001>, <100>, and <010> directions in feldspar (Fig 11b) show a random distribution of points, with no obvious preferred orientation.

These EBSD data highlight the difference in quartz and feldspar behaviour in the sample. Quartz, particularly in the upper domain, forms ribbon grains and has a pronounced CPO, while feldspar consists of smaller, more randomly oriented grains. This suggests that the quartz, especially in the upper left domain has accommodated more of the strain than the feldspar.

Passchier and Trouw (1996) describe how polymineralic aggregates of feldspar and quartz such as a granite will deform heterogeneously because of their different symmetries (Vernon, 2004). Quartz deforms in a ductile manner more readily, tends to accommodate the strain in the rock, and wrap around the feldspar. At low-grade conditions, feldspar still deforms in a brittle manner while quartz deforms by dislocation glide. At higher grades, both deform by dislocation slip processes, but quartz deforms homogeneously while feldspar still deforms less readily, and develops dislocation tangles that will appear as subgrain boundaries. Core-and-mantle structures are also common as the edges of large grains slowly begin to deform more readily.

During dislocation creep, the temperature and strain rate affects which slip systems are active. (Twiss and Moores, 1997). At low grades, quartz slips along the basal plane {0001} <10-10>, and at higher grades, it tends to slip along prism planes, {1-101} <11-20>, and rhomb planes {10-10}<1-210> (see Fig 12a). Feldspar begins to deform by dislocation slip under medium to high grade conditions (Passchier and Trouw, 1996), and changes from c-slip (010)[001] to a-slip (010)[100] with increasing grade or water activity (Ji et al., 2004).

Schmid factor maps

A Schmid factor map shows which grains are favourably oriented for slip on certain planes. Figure 12 (b., c. and d.) show the three previously mentioned slip systems for quartz. Warm colours represent a more favourable alignment. These diagrams indicate strongly that quartz is likely to have slipped along the {10-10} (prism) plane in the direction of <1-210>. Feldspar, on the other hand show no favourable orientation for a or c slip, suggesting that it has resisted intracrystalline deformation.

It is an assumption to state that this rock is deformed by dislocation slip simply based on the existence of a CPO (see Vernon 2004). However, it is a dominant mechanism in quartz, whose high symmetry allows it to deform readily by slip, and it is consistent with the behaviour of quartzofeldspathic rocks at low to medium grade conditions. Dislocation slip is also supported by the favourable orientation for slip and the elongate grain shape of the quartz, and the development of subgrains. It is likely that other mechanisms are important also, such as dislocation climb and cross-slip, which recover dislocation tangles caused by dislocation glide (Knipe, 1989). Because of the small grain size, particularly in the feldspar, it is also likely that deformation takes place by grain boundary sliding (Vernon, 2004). This is especially true in the feldspars that show no evidence for internal strain.

Sample 155731

Sample 155731 is from the centre of the transect on the ridge above Spaghetti Junction (0486733N, 7146105E). It has grainsize around 1-2mm, and the foliation is defined by aligned biotite grains, and, like 155727 possesses bands of elongate quartz, and domains which are

predominantly feldspar. Unlike 155727, relatively strain-free quartz bands run through the sample, and the grain size of the quartz is smaller than that of the feldspar, but still more elongate.

Phases

In this sample, the total proportion of feldspar indexed is higher than that of quartz, and orthoclase and albite make up around half of the feldspar. It should be noted that some feldspar grains show a large number of individual pixels that have been indexed as a different type of feldspar. This is likely to be an artefact of the misindexing of specific feldspars (see previous section) and will artificially skew the number of grains detected within the map (Fig. 13a). No titanite, garnet or amphibole was successfully indexed. There was a high rate of zero solutions (41%), which is in part due to the biotite in the sample (appearing black in the phase map).

Grain boundaries

Quartz shows some development of low angle boundaries, whereas feldspar shows almost none. There is still a high occurrence of Dauphinè twins.

All-Euler map

Quartz displays some related angles (Fig. 13 b and c), shown in green, and the yellow and dark blue colours also represent similar orientations (the colours on an Euler map do not wrap around smoothly), but any preferred orientation is markedly less then the previous sample. The feldspar map shows no clear orientation relationship.

Misorientation histograms

Both the quartz and feldspar histograms (Fig. 14a, b, c, and d) show a pronounced correlation between the theoretical random and the correlated and uncorrelated misorientations, with the exception of Dauphinè twins in the quartz, and a high number of 175-180º angles in all three feldspars. The albite histogram shows a very irregular distribution, but this is probably unreliable as the software only detected 132 neighbouring pairs of albite grains to measure. This suggests poor CPO development in all minerals.

Pole plots

A pole plot of quartz c axes (Fig 15a), with one point per grain shows a wide spread of points, but it could be said to have a broad maximum in the centre of the plot. The feldspar is plotted as anorthite (Fig. 15b), albite (Fig. 15c) and orthoclase (Fig 15d). Even though the histogram and the Euler plot show random distributions, these all show several distinct maxima, and each feldspar shows maxima in a similar location; however, although the software has attempted to plot these as one point per grain, they have been unduly weighted by the irregular feldspar indexing described previously, and so probably do not show real preferred orientation.

Schmid factor maps

The Schmid factor diagrams (Fig. 16 a, b and c) again show that quartz is most favourably aligned with {m}<a> slip, and feldspar again show no preferred slip. The amount of quartz alignment was limited.

One possibility for the lack of CPO could be that the fabric is that this fabric is less well developed than the former (and following) sample. The importance of dislocation slip could be lower, and thus the lack of CPO. However, the granite has undergone considerable grain size reduction and achieved a strong foliation, so it is uncertain that a CPO has not developed as a result of too low strain, where a strong one has developed in other nearby rocks. This could be tested by further EBSD analysis on samples with varying texture development.

Another possibility comes from the observation that there is considerably more biotite within the map. A study of pelites (Rahimi-Chakdel et al., 2006) suggests that the presence of biotite may suppress CPO development in quartz, and this may have occurred with sample 155731, at least locally.

Sample 155718

Sample 155718 is a very fine-grained mylonite sample from the southeast edge of spaghetti hill (0487424N, 7146169E). Its grainsize is up to ~20 microns. Quartz grains are elongate to

polygonal. In the centre of the phase map (Fig. 17a) quartz forms a band of elongate grains, about two grains in width. Throughout the rest of the map it is distributed evenly amongst the feldspars. Feldspar occurs as small even grains.

Phases

Again, the proportion of feldspar indexed is higher than that of quartz, and albite and orthoclase make up half of the total feldspar (Fig. 17 a). This sample also shows some grains of feldspar that have been intermittently assigned more than one type of feldspar. A small proportion of amphibole (2.2%) was indexed. Zero solutions were high (37%).

Grain boundaries

The quartz has considerably more Dauphinè and high angle boundaries than low angle boundaries (Fig.17a). Feldspar shows some formation of high angle boundaries, but few to no low angle boundaries.

The all-Euler angle maps (Fig.17 b and c) show that most of the quartz, especially the band in the centre, has a related CPO. Feldspars still seem to have a fairly unrelated orientation, although there does seem to be some prevalence of warm colours on the map.

Misorientation Histogram

Misorientation histograms (Fig. 18a and b) show that the correlated and uncorrelated misorientation angles for this sample are similar to the theoretical random, however the quartz still demonstrates the 60º peak made by the Dauphinè twins, and there is a small increase in low angle boundaries.

Pole plots

The c axis of quartz in sample 155718 has a small spread of points, but there is a strong single maximum parallel to the y axis of the sample (Figs. 19 a and b) and the a axes are distributed around the edge of the stereonet. Feldspar shows highly random orientation.

Schmid factor maps

As may be expected from the pole plots, the Schmid factor maps (Fig. 20a, b and c) show that quartz is almost universally oriented favourably for slip along the {1-101}<1-210> prism plane.

Because the quality of these last two analyses is considerably lower than the first one, considerably less confidence can be placed in them. However, they seem to support the conclusions drawn from sample 155727. All show a contrast in behaviour of quartz and feldspar, which is consistent with their different strengths and symmetry.

6.Thermobarometry

Mineral composition analyses of samples for determining the pressure-temperature history of the field area were made on the Adelaide Microscopy Cameca SX51 Microprobe, operating with an accelerating voltage of 15kV, and beam current of 20nA and a spot size of 4. Representative microprobe analyses are presented in Table 1. Additional cation mapping of the two largest garnets was carried out for the elements Ca, Mn, Mg and Fe at an accelerating voltage of 15kV and a beam current of 100nA.

Mineral Chemistry

Garnet is almandine rich, (typically X_{Fe} (Fe/Fe+Mg+Ca+Mn)=0.45-0.57), with moderate grossular content (X_{Ca}=0.35-0.24). Larger garnets show minor zoning (see Fig 21), with garnets increasing in pyrope content at the rims, however, samples never have more pyrope than X_{Mg} =0.09. Hornblende end members in the sample were pargasite, tschermackite, tremolite, ferroactinolite and glaucophane. Hornblende typically has an X_{Mg} (Mg^{+}/Fe^{2+}+Mg)=0.32-0.44. Biotite typically has an X_{Fe} (Fe/Fe+Mg) of 0.48-0.63.

Plagioclase is generally sodic, and has a composition Ab_{73-76}. Orthoclase is less common, but present in all samples.

Activities for the mineral data collected were calculated using the program AX (Powell, 1998) and average temperatures and pressures were obtained using THERMOCALC (Powell and Holland, 1988). Representative output files are shown in Appendices 1 and 2.

THERMOCALC was chosen because it uses as many independent reactions as possible, and propagates errors throughout the calculation process (Powell and Holland, 1994), however using different thermobarometers may result in different pressure-temperature estimates (Scrimgeour and Close, 1999) which is important to note when comparing with previous estimates.

Results

Using the assemblage garnet + hornblende + plagioclase + orthoclase + biotite + ilmenite + magnetite + titanite + quartz produces an estimate range of 590-860˚C and 6-12kbars for all the samples using the average pressure-temperature approach of Powell and Holland (1994) (Table 2). Average P-T estimates were made with water removed from the system because the water activity had a considerable effect on the result. Table 3 shows average pressure calculations for sample 155716, varying the water activity between 0.2 and 0.8. This changes the estimate by more than 1Kbar.

If including water as a phase in average PT calculations, high values of water activity between 0.8 and 1 most closely resemble the dry average PT calculation results (see Table 4; apart from sample 155718) but these values rarely fit within 95% confidence. In addition, removing water from the analysis significantly increases the error.

The variation in pressure and temperature calculations is not reflected in the spatial distribution of the samples. Related samples, eg. 155716 and 155717 have pressure-temperature estimates of 644±298ºC and 11.7±2.5 kbars and 589±220ºC and 9.6±1.9 kbars respectively. However, these values are within error of each other, and as they are likely to have experienced the same P-T conditions, an average of the most precise results are here quoted as ~11 kbars and ~700ºC.

7. SHRIMP U-Pb Geochronology

U-Pb isotope measurements were made on zircon and titanite extracted from within the shear zones on Spaghetti Hill. Sample 155737 is a coarse protomylonite sample from the west end of Spaghetti Junction from a northwest trending shear zone. Sample 155735 is from a fully developed mylonite from the west edge of Spaghetti Junction, from a shear zone that trends in the same direction as 155735, but dipping in the opposite direction. Sample 155731 is a fine-grained mylonite from the transect on the western ridge, running northeast.

Zircons extracted are colourless or light tan, up to 200*μ*m across, up to 500*μ*m long, and are present in several morphologies (Fig. 22). These were predominantly highly elongate grains with rounded ends, but also large, stubby grains, and very small, semi-prismatic grains. Most grains are euhedral and preserve igneous zoning patterns involving alternating high- and low-CL layering. A majority of the zircon crystals have euhedral cores picked out by with low or high CL, mantled by several layers. The inner layers are formed from euhedral zircon largely concordant with the core, and which preserves concentric banding and has low a CL response. In a majority of the zircon grains, the unzoned rim truncates igneous banding in the core or intermediate layer. The rims typically have moderate to high CL responses.

The titanites are clear to light brown, up to 500μm in length. They are oval shaped and appear as small porphyroblasts throughout the matrix.

Analytical techniques

Crushing and mineral separation were performed in the mineral separation laboratory at the University of Adelaide, South Australia. Fist-sized portions of rock were cut from the samples and crushed using a tungsten carbide ring mill. The crushed sample was then sieved and the 75–300 *μ*m fraction (125-300 *μ*m for the titanite) was washed to remove dust. Zircon and titanite were separated using a combination of panning, heavy liquid and Franz magnetic methods. Approximately 100 representative zircon from samples 155735 and 155737, and 100 titanites from sample 155734 were handpicked and mounted, with several grains of standard zircon, in a 2.5 cm diameter epoxy mount. The mount was polished until the grains were sectioned to approximately half of their diameter. The sample was then photographed in

transmitted and reflected light to reveal inclusions and zoning in the zircon. Zircon grains were imaged and their internal structures investigated using standard BSE and CL imaging techniques using a Phillips XL20 SEM with attached Gatan CL operated at 12 keV at Adelaide Microscopy.

Zircon and titanite data was collected using the Sensitive High Resolution Ion MicroProbe (SHRIMP II) in the John de Laeter centre for Mass Spectrometry at Curtin University, Perth, Australia.

SHRIMP operating procedures used for U, Th and Pb isotope measurement in zircon are outlined by (Compston et al., 1992) and (Williams et al., 1984). To reduce surficial common lead, each analysis spot was rastered with the ion beam for 3-5 minutes prior to analysis. Measured ^{204}Pb on the CZ3 standard zircon was typically between 3 and 13 ppb, and is attributed to common lead on the mount surface. All Pb/U and Pb/Pb ratios quoted in the tables and discussed in the text have been corrected for common lead.

In total there are 8 analyses of 7 zircons from sample 155737. Pb^{207}/Pb^{206} ratios of sample 155737 yields an age of 1137±13Ma (MSWD = 0.96). This is interpreted as being the age of the granite crystallisation. Cores and rims analysed revealed similar ages (eg see Fig. 22)

Figure 23 (a, b and c) shows the concordia plots of the three samples. 14 analyses of 11 zircons were obtained from sample 155735. The concordia plot of this sample shows two populations, Pb^{207}/Pb^{206} ratio of these at 1121±11Ma (MSWD=1.58), which is interpreted as the crystallisation age of the granite and Pb^{206}/Pb^{238} ratio of the other one at 570±25Ma (MSWD=1.4), which is interpreted as deformation during the Petermann Orogeny. Different ages are quoted for younger analyses as the Pb^{206}/Pb^{238} age is more precise for younger ages as the half life of U^{238} is longer than that of U^{235}.The 1089Ma ages came from cores and from large, low CL rims. The 570±25Ma age came from large high CL rims on subhedral zircons.

10 analyses of titanites from sample 155731 yield an age of 523±14Ma (MSWD=0.87), which is also interpreted as being from the Petermann Orogeny.

8.Discussion

Age of the Petermann Orogen and Spaghetti Hill deformation

The duration of the Petermann Orogeny is poorly constrained between ~560-520Ma by one zircon age and Sm-Nd dating from the Northern Territory (eg Edgoose et al. 2004, 2004, Clark et al. 1995), although (Wade et al., 2005) has suggested that deformation may have commenced as early as 600Ma based on the influx of sediment into the Officer Basin.

The results obtained from Spaghetti Hill zircon of 570±25Ma, from titanite of 523±14Ma are both reasonable ages for Petermann Deformation. While these ages were obtained from samples close by each other because of the small field area, they represent the opposite ends of the Petermann Orogeny. The ages are outside 2σ error, suggesting that these either date two events, or two parts of P-T evolution. Camacho et al (1997) also obtained a 522Ma age from Ar^{40}-Ar^{39} dating of muscovite in the Northern Territory. This implies a lower temperature at the same age obtained from the Spaghetti Hill titanites, however this date is from the eastern end of the Musgraves.

PT estimates of Petermann Orogen and Spaghetti Hill

Figure 1b shows a map of the distribution of previous pressure-temperature results throughout the Musgrave Block.

In the Western Musgraves, Clarke et al (1995) reported 10-14kbars at 600-750ºC in mylonites from the Petermann Orogeny in the Champ de mars and Mt Aloysius areas. In the Mann Ranges, Northern Territory, Scrimgeour et al. (1999) report peak estimates of 12-14 kbars and 700-750ºC. North of the Mann Ranges, they obtained results of 6-7 kbars and 650ºC. Camacho et al. (1997) measured eclogite facies rocks in the Davenport Shear zone, Musgrave Ranges at12kbars and 650ºC.

The results obtained from Spaghetti Hill are in the range of 590-860˚C and 6-12kbars. This is a very broad spread, however, only one of them is below 640ºC and only one of them is above

790ºC. The pressure estimates show a similarly broad spread. The results from Spaghetti Hill have large errors, but are still within error of results by other authors.

The resetting of titanite, whose closure temperature may be up to 660ºC (Frost et al, 2000) and Argon temperatures between 300 and 640 degrees in the eastern Musgraves (Camacho et al., 1997) during the Petermann Orogeny provide some lower constraints on the temperature.

A possible upper constraint on the temperature comes from the absence of melting in the samples, suggesting an upper limit of ~800ºC (Winter, 2001). However, there are occurrences of migmatite on nearby outcrops.

The errors on these results are large. This could be attributed to insufficient equilibration between analysed minerals, given that garnets showed prograde zoning, and the fabric of the samples wraps around the garnet.

Structure of Petermann Orogen and Spaghetti Hill

The Petermann Orogeny is generally described as a north-directed orogen, as the Petermann Nappe has been thrust north over 100km (Flottmann et al., 2004). Thus, Petermann-age structures in the Musgraves are commonly described as having north-directed movement (eg the Woodroofe Thrust, Davenport Shear Zone, and the Mann Fault (Stewart, 1995). Only Kelly et al. (2006) describes southeast and southwest movement in post-800Ma, pre-Petermann deformations D4 and D5. It is highly probable that these are also Petermann events. In contrast to most studies, shear zones in Spaghetti Hill clearly demonstrate south-southwest directed movement. This is commonly found throughout the western Musgraves (Smithies, 2006 pers. comm.). Edgoose et al. (2004) describe the Petermann Orogeny in the Musgrave Block as being part of a flower structure, and this model would account for north- and south-directed transport during the same deformation.

Structural and Thermal evolution of Spaghetti Hill in the Neoproterozoic

If the date provided by U-Pb zircon analysis is taken to be the age of peak deformation, and the date provided by the titanite is assumed to be the date at which the rock cooled below the titanite closure temperature, then the cooling history of this rock implies that it took 50 million years to cool between at most 200ºC and at least 50ºC (1-4ºC/Ma). This is a very slow cooling rate, but it should be noted that it does not take into account the errors on the ages, and could in fact be much faster, or slower if the age errors were considered.

Scrimgeour et al. (1999) report both slow and fast-cooling regions of the Northern Musgraves for the Petermann Orogeny. In these regions the thermal gradient is inferred to be 17ºC/km, in the Mann Ranges and 30-35ºC/km north of Woodroofe Thrust. Similar to the Mann Ranges, Camacho (1997) describes 16ºC/km at 550 Ma and 18ºC/km at 535Ma for the southeastern Musgraves. Both report that the lower geothermal gradients are similar to other stable Proterozoic cratons.

Estimates for the geothermal gradient for Spaghetti Hill during the Petermann Orogeny, based on P-T calculations average 21ºC/km, assuming a pressure gradient of 0.3kbars per kilometre (Winter, 2001) and without taking the errors into account. This is closer to the slower cooling gradient reported above, suggesting that the heat flow is slightly higher than average, and not compatible with the slow cooling rate inferred from the geochronological results.

There are some possibilities that negate the necessity of such slow cooling. The first is that there were two deformation events, resulting in the two different ages. The zircon samples were taken from Spaghetti Junction, and the titanites from the transect on the ridge above Spaghetti Junction, and these shear zones have different orientations. However, this would imply two deformations with similar PT conditions. Furthermore, the shear zones appear to be of the same generation, and no crosscutting relationships were observed. The strain is also compatible with one event, with the same sense of movement and lineation.

The next possibility is that there is very slow cooling during a long protracted deformation, with the zircons preserving deformation ages. At maximum 2σ error, the cooling rate would be 100ºC in around 47 million years, i.e. a cooling rate of around 2ºC per million years. Camacho et al. (1997) estimated a cooling rate of 4ºC based on the closure temperature of Sm-Nd and Ar-Ar systems, twice the rate suggested by the Spaghetti Hill dates.

The last possibility is that the age recorded by the titanite is from a lower temperature than its closure temperature. Because metamorphic systems contain titanium and calcium, unlike zircon, titanite continues to react after it has been reset. The age it yields is then a metamorphic crystallisation age (Frost et al., 2000). This would allow a much faster cooling rate.

However, the well-developed fabric appears to be from peak conditions, and the mineral assemblages from which PT estimates were made had garnet that preserved prograde zoning. The highest temperature garnet rims are interpreted as being in equilibrium with the surrounding minerals in the matrix, including titanite. Garnet cation zoning is preserved when it cools faster than it can equilibrate. (Winter, 2001) If the rocks at Spaghetti Hill experienced non-linear cooling, first fast cooling, then slower cooling, this would account for the garnet texture, and the long time span over which it cooled.

9.Conclusion

Granite from Spaghetti Hill yields protolith crystallisation ages of 1137±13 and 1121±11Ma. These rocks were deformed by the Petermann Orogeny. This deformation was south directed and reached peak conditions of ~700ºC and 11kbars at around 570±25Ma, followed a non-linear cooling path and cooled below titanite closure temperature by 522±14Ma.

10.Acknowledgements

I thank Alan Collins, Hugh Smithies and Heather Howard of GSWA for help and wisdom, Mario Holmes for tyre lessons, the wizards at Adelaide Microscopy, and Simon Bodorkos from GSWA, Steve Reddy from Curtin, for much needed technical assistance. Mike Belperio for

toasties and good music in the bush, and honours students of 2006. Last of all, thanks to Louise, Dave, Stacey, Peter, Harry and Spike.

11.Appendices

Appendix 1: representative AX output file

```
Calculations for P = 8.0 kbar and T =  650°C
_____________________________________________________________________
_______

g  716gt2_1
2-site mixing + Regular solution gammas
Ferric from:  Cation Sum = 8 for 12 oxygens
W: py.alm=2.5, gr.py=33, py.andr=73, alm.andr=60, spss.andr=60 kJ

oxide     wt %    cations    ±sd             activity                 ±sd
±%

SiO2    36.96    2.987    0.036         py      0.00065    0.000244    38
TiO2    0.00    0.000    0.003         gr      0.037      0.0074      20
Al2O3   19.65   1.872   0.029          alm     0.111      0.013       12
Cr2O3    0.06    0.004    0.003        spss    0.00064    0.000241    38
Fe2O3    2.68    0.163    0.064        andr    0.01907    0.004609    24
  FeO   21.37    1.444    0.054
  MnO    3.81    0.261    0.007
  MgO    1.26    0.152    0.008
  CaO   12.77    1.106    0.020
  Na2O   0.06    0.010    0.008
  K2O    0.02    0.002    0.005

totals  98.37    8.000
```

Appendix 2: Example output file from THERMOCALC

```
calculation type :
     0 = table of thermodynamic data of end-members
     1 = phase diagram calculations
     2 = average pressure-temperature calculations
     3 = calculations on all reactions between end-members
     4 = list end-member names and compositions
control code  : 2
data filename: suffix in 'tcd.txt' : 716
datafile being read: "tcd716.txt"
reading phase info from this file ...
py  gr  alm  spss  andr  an  ab  tr  parg  gl  mt  usp  phl  ann  east  q
H2O  sph  san
log output is in "tclog.txt"
main output is in the file, "tco716.txt"
other (eg drawpd) output is in the file, "tcdr.txt"

THERMOCALC 3.26  running at 10.56 on Fri 22 Sep,2006, with
tcds55.txt produced at 19:29:59 on 22 Nov 2003 (with sigma fit =  1.067)


py  gr  alm  spss  andr  an  ab  tr  parg  gl  mt
usp  phl  ann  east  q  H2O  sph  san
which end-members : (nothing input)

spss excluded
type of rock calculation:
       1 : average P
       2 : average T
       3 : average PT
code : 2

             py       gr      alm     andr       an       ab       tr     parg       gl
mt
     a 0.000650   0.0370    0.111   0.0191    0.340    0.770  0.00229  0.00280  4.31e-6
0.370
 sd(a) 0.000488   0.0148   0.0270  0.00922   0.0444   0.0385  0.00124  0.00199  4.15e-5
0.0370

            usp      phl      ann     east        q      H2O      sph      san
     a    0.150   0.0470   0.0560   0.0280     1.00             1.00    0.900
 sd(a)   0.0338   0.0173   0.0192   0.0116        0                0   0.0450

these data ok ? no
names of end-members to be excluded : east
these are the only changes you want to make ? yes
rock was fluid-bearing ? no

specification of PT window:
P range over which average T to be calculated
P window: P low,high :  8 12
T window within which average T expected to lie
T window: T low,high :  500 700
P window :8 <-> 12 kbar :P interval : 1
fixed a(H2O) : .2

Reactions must be reasonably linear within the window;
allowed angle change of reaction per 25¡C (try 1) : 1
reactions :
|0|0|0|000XX|00000000000000000000000000|0|X|0|----------|00000000000
0000:0X0-0X------|00:0|0:00|0000000000000000000000000000000000000000000000|:000000
00::00000000000000000000000:00000000000|00000|-|--000-0:-0--00-00X-------------
--------------------------------------------------------------------------------
--------------------------------------------------------------------------------
--------------------------------------------------------------------------------
--------------------------------------------------------------------------------
------------------------------|00000000000000000000X

an independent set of reactions has been calculated

Activities and their uncertainties

                py       gr      alm     andr       an       ab       tr
a          0.000650   0.0370    0.111   0.0191    0.340    0.770  0.00229
```

sd(a)/a	0.75083	0.40013	0.24281	0.48334	0.13068	0.05000	0.54400

	parg	gl	mt	usp	phl	ann
a	0.00280	4.31e-6	0.370	0.150	0.0470	0.0560
sd(a)/a	0.71142	9.63366	0.10000	0.22524	0.36805	0.34308

	q	H2O	sph	san
a	1.00	0.200	1.00	0.900
sd(a)/a	0		0	0.05000

Independent set of reactions
1) 2gr + 7phl + 24q = 2py + 3tr + 4H2O + 7san
2) 6an + 11phl + 30q = 6py + 3tr + 8H2O + 11san
3) py + ann = alm + phl
4) 3parg + 4phl + 24q = 3py + 3ab + 3tr + 4H2O + 4san
5) 6gr + 6an + 6ab + 3gl + 13phl = 12parg + 4H2O + 13san
6) 16alm + 15phl + 24sph = 10py + 6gr + 3tr + 24usp + 12H2O + 15san
7) 3gr + 3mt + 2phl + 9q = 2py + alm + 3andr + 2H2O + 2san

Calculations for the independent set of reactions
at P = 10.0 kbar (for a(H2O) = 0.2)

	T(P)	sd(T)	a	sd(a)	b	c	ln_K	sd(ln_K)
1	533	72	290.83	2.80	-0.35460	3.289	-5.661	3.510
2	530	102	611.71	4.33	-0.45562	-9.042	-23.327	6.346
3	593	507	-44.60	0.92	0.01351	-0.287	4.965	0.936
4	638	111	312.31	3.33	-0.25051	0.356	-11.599	3.811
5	545	286	342.09	12.29	-0.77721	7.129	32.727	30.626
6	649	81	1334.13	19.67	-1.09398	26.814	-77.485	11.839
7	586	127	220.21	1.84	-0.14633	-2.323	-9.976	2.549

Average temperatures (for a(H2O) = 0.2)

av T at 8.0 kbar,
av T at 9.0 kbar,
av T at 10.0 kbar,

corresponding average T

	avT	sd	fit
lsq	651	56	1.43

diagnostics on this average T

for 95% confidence, fit (= sd(fit) = sqrt(MSWD)) < 1.45 (but larger may be OK)

column:
1-3: result of doubling the uncertainty on ln a.
4: e* = ln a residuals normalised to sd(ln a) : |e*| >2.5 suspect?
5: hat = diagonal elements of the hat matrix : hat >0.41 influential.
6-7: observed and calculated activities of endmembers.
8-9: regression-through-origin x,y values

	T	sd	fit	e*	hat	a(obs)	a(calc)	x	y
py	654	57	1.42	0.3	0.07	0.000650	0.000836	0.01	5.89
gr	652	56	1.42	-0.3	0.01	0.0370	0.0324	-0.00	-2.08
alm	640	52	1.31	1.2	0.03	0.111	0.149	-0.00	-5.34
andr	646	58	1.42	-0.4	0.07	0.0191	0.0157	0.01	6.73
an	645	52	1.33	-0.9	0.01	0.340	0.302	0.00	2.97
ab	651	56	1.43	-0.1	0.00	0.770	0.765	0.00	0.18
tr	658	58	1.41	0.5	0.09	0.00229	0.00293	0.01	6.61
parg	649	49	1.27	1.7	0.00	0.00280	0.00943	-0.00	-2.41
gl	651	55	1.41	0.6	0.00	4.31e-6	0.00216	-0.00	-1.08
mt	650	56	1.43	0.1	0.00	0.370	0.373	-0.00	-1.39
usp	604	62	1.27	-1.2	0.34	0.150	0.114	0.01	14.97
phl	694	49	1.12	-1.9	0.20	0.0470	0.0235	-0.01	-8.64
ann	659	57	1.41	-0.6	0.08	0.0560	0.0464	-0.01	-6.07
q	651	56	1.43	0	0	1.00	1.00	0	0
H2O	651	56	1.43	0	0	1.00	1.00	0	0
sph	651	56	1.43	0	0	1.00	1.00	0	0
san	655	56	1.41	0.3	0.01	0.900	0.900	0.00	2.06

av T at 11.0 kbar,
av T at 12.0 kbar,

P	8.0	9.0	10.0	11.0	12.0
av T	609	630	651	672	691

```
sd          46    48    56    68    82
sigfit     1.2   1.2   1.4   1.7   2.1

more calculations with this rock ? no
```

12.Figure Captions

Figure 1. (a, upper) The Musgrave Block, showing the position of the Mann Fault; (b, lower) Detail map showing P-T estimates from Clarke et al, 1995 (Western Australia), Scrimgeour et al., 1999 (Northern Territory) and Camacho et al., 1997 (Southeastern Musgraves).

Figure 2. Structural Map of Spaghetti Hill, Detailed map of Spaghetti Junction (inset) shows level of mylonitisation. Inset: structural readings: lineations (stars) and foliations(squares) .

Figure 3. Rotated feldspar porphyroblast showing sinistral (top-to the southwest) movement. Picture facing northwest.

Figure 4. Folds in a) central and b) eastern Spaghetti Junction.

Figure 5. Rotated garnet porphyroblast (sample 155727).

Figure 6. Schematic diagram showing sample transect, with relative thicknesses of zones, and sample locations.

Figure 7. Change in Feldspar shape.Feldspar changes from round or oval to highly elongate.

Figure 8. Photographs from transect: a)undeformed granite; b)Mylonite; c)Intermediate; d) Protomylonite, facing southeast.

Figure 9. Sample 155727a) Phase boundary map and grain boundaries superimposed on band contrast. Quartz=green; Anorthite=Aqua; Albite=blue; Orthoclase=teal. Dauphine twins=yellow; low angle (2º-10º) boundaries=red; High angle (>10º) boundaries=black. b)All Euler map of quartz; c)all Euler map of feldspar.

Figure 10. Misorientation Angle Distribution of a)quartz and b)anorthite.

Figure 11. Pole plots and contours for a) quartz c and a axis and b) feldspar, <001>, <010> <100>, using one point per grain subset.

Figure 12. a) Quartz crystal showing prism (m) and rhomb (r) planes. b) Schmid factor maps for quartz of b) [1-210]<10- 10>, c) [1 -101]<11-20>, and d)[0001]<10-10>. Cool colours represent unfavourable orientations; warm colours represent favourable orientations.

Figure 13. a)Phase and grain boundary map of sample 155731 Quartz=green, anorthite=aqua, albite=blue, orthoclase=teal. Grain boundaries: yellow=Dauphinè twins, red= 2-10º boundary, black=>10º b) All Euler map of quartz, c) all Euler map of feldspar.

Figure 14. Misorientation angle distributions for sample 155731 a)quartz, b)anorthite, c)albite and d)orthoclase.

Figure 15. Pole figures and contours of a) quartz c axis <0001> and a axis <10-10>, and b) Anorthite, c) Albite, d) Orthoclase, each showing <001>, <100>, and <010>. Anorthite requires upper and lower hemispheres to describe the orientation of the axes.

Figure 16. Quartz Schmid Factor diagrams showing slip systems a){10-10}<1-210>; b;{1-101}<11-20> and c){0001}<10-10>. Warm colours represent favourable orientation for slip on that plane, cool colours represent unfavourable orientation.

Figure 17. a)Phase and grain boundary images of sample 155718. Quartz=green, Anorthite=aqua, Albite=blue, Orthoclase=teal. Grain boundaries: yellow= Dauphine twins, red=2º-10º, black=>10º. b) All Euler map of quartz; c) All Euler map of feldspar.

Figure 18. Misorientation angle distribution from a) quartz and b) anorthite.

Figure 19. Pole figures and contours of a) quartz c axis <0001> and a axis <10-10>, and b) Anorthite, c) showing <001>, <100>, and <010>. Anorthite requires upper and lower hemispheres to describe the orientation of the axes.

Figure 20. Quartz Schmid Factor diagrams showing slip systems a) {10-10}<1-210>; b){1-101}<11-20> and c) {0001}<10-10>. Warm colours represent favourable orientation for slip on that plane, cool colours represent unfavourable orientation.

Figure 21. a) sample 155716 and b) sample 155717: Cation maps of garnet showing zoning patterns of Ca, Fe, Mg and Mn. Light colours represent higher values. c) and d) Garnet probe traverses showing relative abundance of Ca, Fe, Mg and Mn. Traverse Locations are shown as white lines on Ca map for both garnets. For 155717, points are from the edge in.

Figure 22. CL images of analysed zircons showing the spot from which the analysis was obtained, and the age (Ma).

Figure 23. Concordia and Weighted Average of a) titanite SHRIMP data, sample 155731 b) Sample 155735, c) Sample155737.

13. References

Camacho, A., Compston, W., McCulloch, M. and Ian, M., 1997. Timing and exhumation of eclogite facies shear zones, Musgrave Block, central Australia. Journal of Metamorphic Geology, 15: 735-751.

Camacho, A. and Fanning, C.M., 1995. Some isotopic constraints on the evolution of the granulite and upper amphibolite facies terranes in the eastern Musgrave Block, central Australia. Precambrian Research, 71: 155-181.

Clarke, G.L., Buick, I.S., Glickson, A.Y. and Stewart, A.J., 1995. Structural and pressure-temperature evolution of host rocks of the Giles Complex, western Musgrave Blick, central Australia: evidence for multiple high-pressure events. Journal of Australian Geology and Geophysics, 16(1): 127-146.

Compston, W., Williams, I., S., Kirschvink, J.L., Zichao, Z. and Guogan, M.A., 1992. Zircon U-Pb ages for the Early Cambrian time-scale. Journal of the Geological Society of London, 149: 171-184.

Edgoose, C.J., Scrimgeour, I.R. and Close, D.F., 2004. Geology of the Musgrave Block, Northern Territory. 15, Northern Territory Geological Survey.

Flottmann, T., Hand, M., Close, D.F., Edgoose, C.J. and Scrimgeour, I.R., 2004. Thrust tectonic styles of the intracratonic Alice Springs and Petermann Orogenies, Central Australia. In: K. McClay (Editor), Thrust tectonics and hydrocarbon systems. The American Association of Petroleum Geologists, Oklahoma, pp. 538-557.

Frost, R., B., Chamberlain, K.R. and Schumacher, J., C., 2000. Sphene (titanite): phase relations and role as a geochronometer. Chemical Geology, 172: 131-148.

Glickson, A.Y., Stewart, A.J., Ballhaus, C.G., Clarke, G.L., Feeken, E.H.J., Leven, J.H., Sheraton, J.W. and Sun, S.-S., 1996. Geology of the western Musgrave Block, central Australia, with particular reference to the mafic-ultramafic Giles Complex. 239, Australian Geological Survey Organisation.

Ji, S., Jiang, Z., Rybacki, E., Wirth, R., Prior, D.J. and Xia, B., 2004. Strain softening and microstructural evolution of anorthite aggregates and quartz-anorthite layered composites deformed in torsion. Earth and Planetary Science Letters, 222: 377-390.

Kelly, N., M., Clarke, G.L. and Harley, S.L., 2006. Monazite behaviour and age significance in poly-metamorhphic. Lithos, 88: 100-134.

Knipe, R.J., 1989. Deformation Mechanisms- recognition from natural tectonites. Journal of Structural Geology, 11(1/2): 127-146.

Neumann, B., 2000. Texture development of recrystallised quartz polycrystals unravelled by orientation and misorientation. Journal of Structural Geology, 22: 1695-1711.

Passchier, C.W. and Trouw, R.A.J., 1996. Microtectonics. Springer, Berlin.

Powell, R., 1998. Calculating phase diagrams involving solid solution via non-linear equations with examples from THERMOCALC. Journal of Metamorphic Geology, 16: 577-585.

Powell, R. and Holland, T., 1988. An internally consistent dataset with uncertainties and correlations:three applications and methods, worked examples and a computer program. Journal of Metamorphic Geology, 6: 173-204.

Powell, R. and Holland, T., 1994. Optimal geothermometry and geobarometry. American Mineralogist, 79: 120-133.

Prior, D.J., Boyle, A.P., Brenker, F., Cheadle, M.C., Day, A., Lopez, G., Peruzzo, L., Potts, G.J., Reddy, S., Speiss, R., Timms, N.E., Trimby, P., Wheeler, J. and Zetterstrom, L., 1999. The application of electron backscatter diffraction and orientation contrast imaging in the SEM to textural problems in rocks. American Mineralogist, 84: 1741-1759.

Rahimi-Chakdel, A., Boyle, A.P. and Prior, D.J., 2006. Quartz deformation mechanisms during Barrovian metamorphism: Implications from crystallographic orientation of different generations of quartz in pelites. Tectonophysics, in press(xx): xx.

Scrimgeour, I.R. and Close, D.F., 1999. Regional high-pressure metamorphism during intracratonic deformation: the Petermann Orogeny, central Australia. Journal of Metamorphic Geology, 17: 557-572.

Stewart, A.J., 1995. Western extension of the Woodroofe Thrust, Musgrave Block, central Australia. Journal of Australian Geology and Geophysics, 16: 1/2.

Twiss, R.J. and Moores, E.M., 1997. Structural Geology. W. H. Freeman and Company, New York.

Vernon, R.H., 2004. A practical guide to rock microstructure. Cambridge University Press, Cambridge.
Wade, B., P., Hand, M. and Barovich, K., M., 2005. Nd isotopic and geochemical constraints on provenance of sedimentary rocks in the eastern Officer Basin, Australia: implications for the duration of the intracratonic Petermann Orogeny. Journal of the Geological Society of London, 162: 513-530.
Wheeler, J., Prior, D.J., Jiang, Z., Speiss, R. and Trimby, P., 2001. The petrological significance of misorientations between grains. Contributions to Mineral Petrology, 141: 109-124.
White, R.W., Clarke, G.L. and Nelson, D.R., 1999. SHRIMP U-Pb zircon dating of Grenville-age events in the Western part of the Musgrave Block, central Australia. Journal of Metamorphic Geology, 17: 465-481.
Williams, I.S., Compston, W., Black, L.P., Ireland, T.R. and Foster, J.J., 1984. Unsupported radiogenic Pb in zircon: a cause of anomalously high Pb-Pb, U-Pb and Th-Pb ages. Contributions to Mineralogy and Petrology, 88: 322-327.
Winter, J.D., 2001. An introduction to igneous and metamorphic petrology. Prentice Hall, New Jersey.

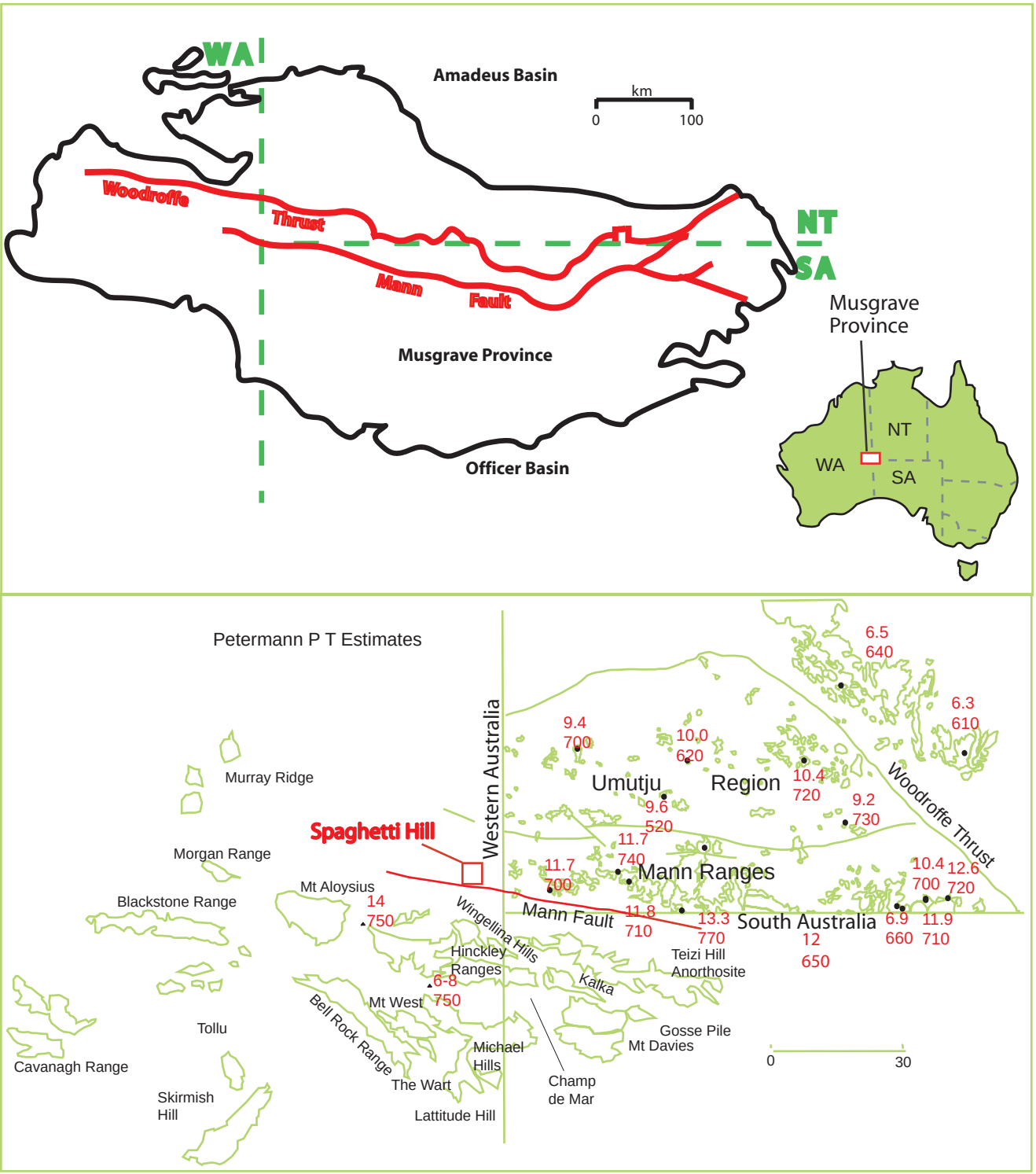

Figure 1 (a, upper) The Musgrave Block, showing the position of the Mann Fault; (b, lower)Detail map showing P-T estimates from Clarke et al, 1995 (Western Australia), Scrimgeour et al., 1999 (Northern Territory) and Camacho et al., 1997 (Southeastern Musgraves).

Spaghetti Hill

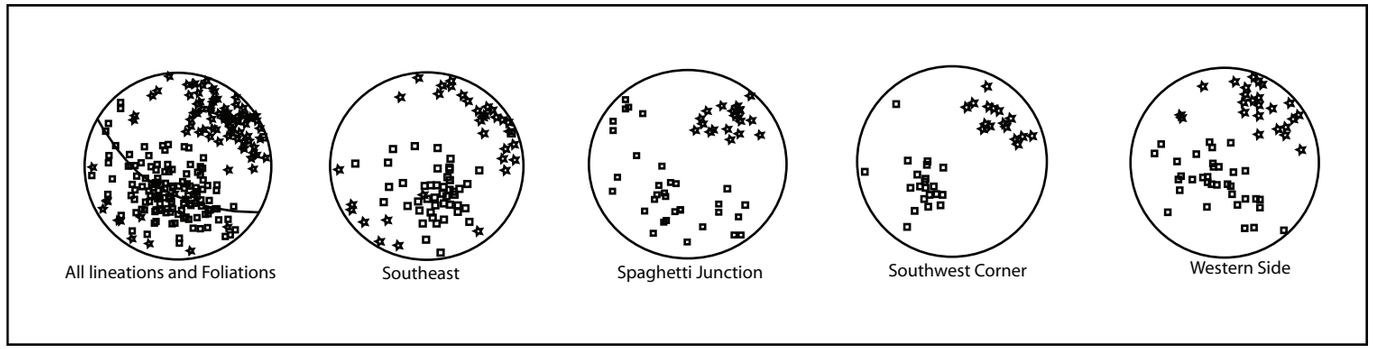

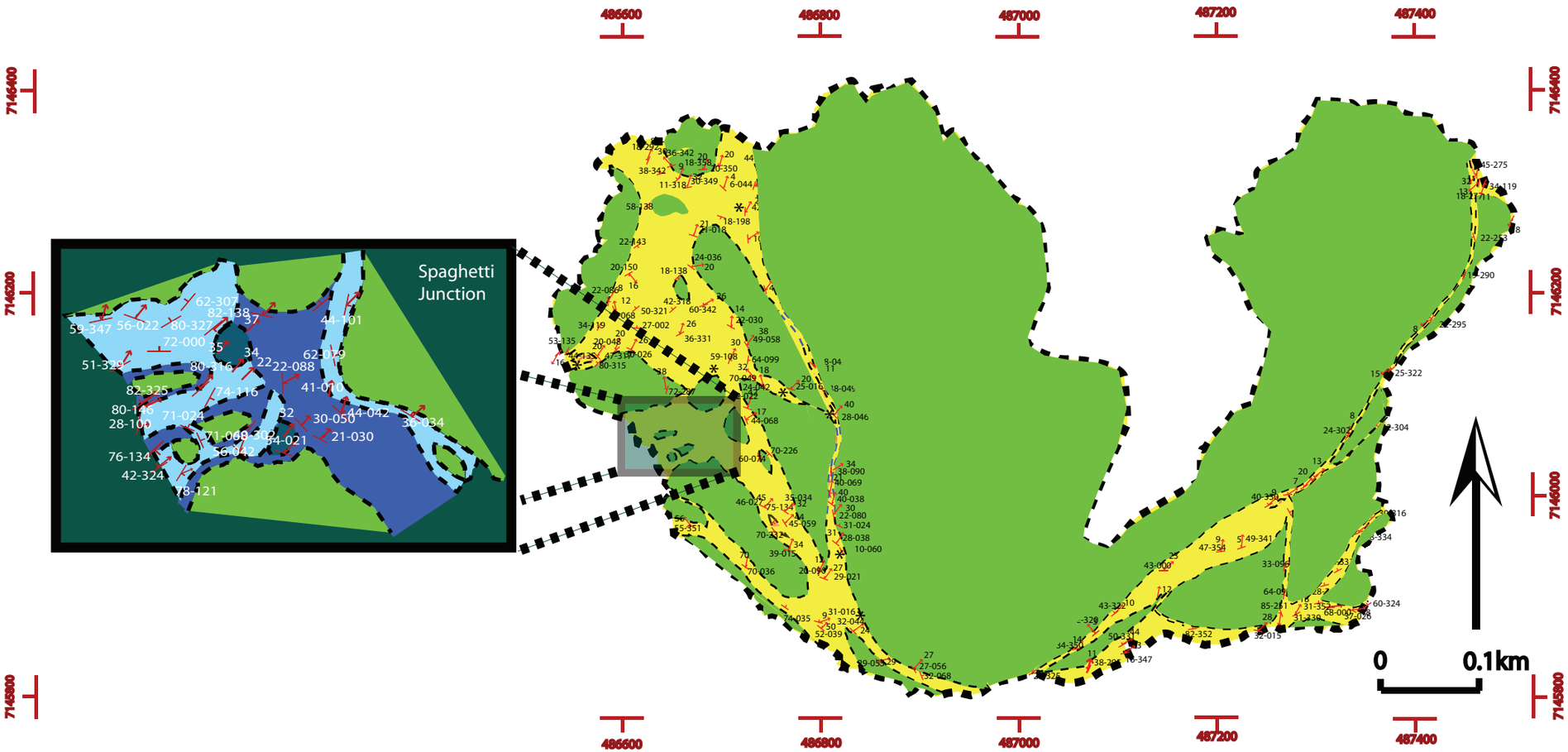

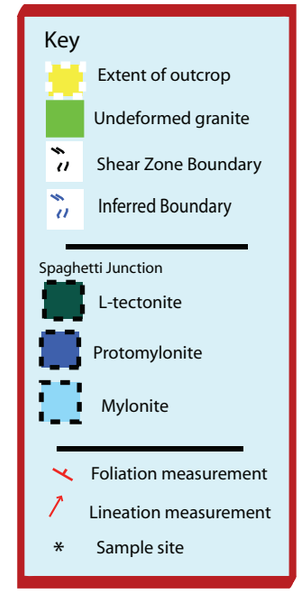

Figure 2.

Figure 3. Rotated feldspar porphyroblast showing sinistral (top-to the southwest) movement. Picture facing northwest.

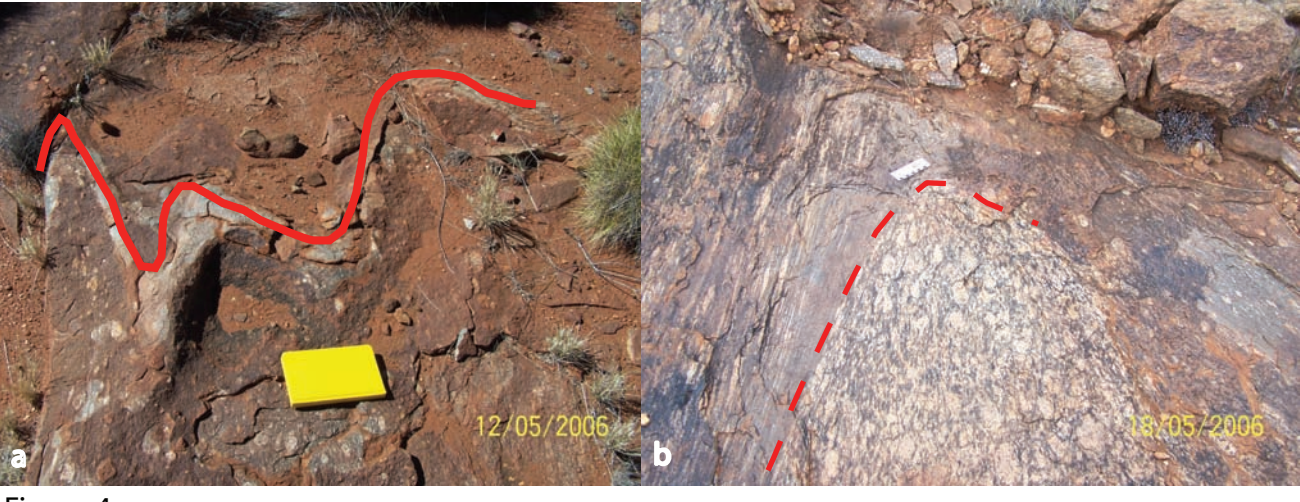

Figure 4.

Figure 5.

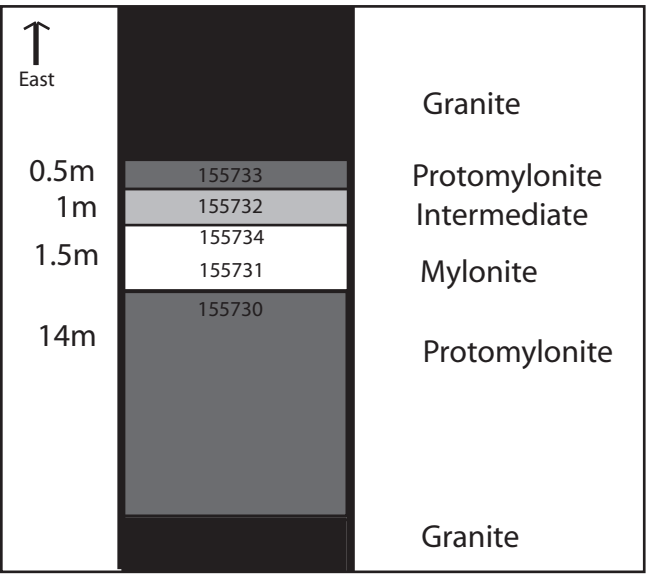

Figure 6.

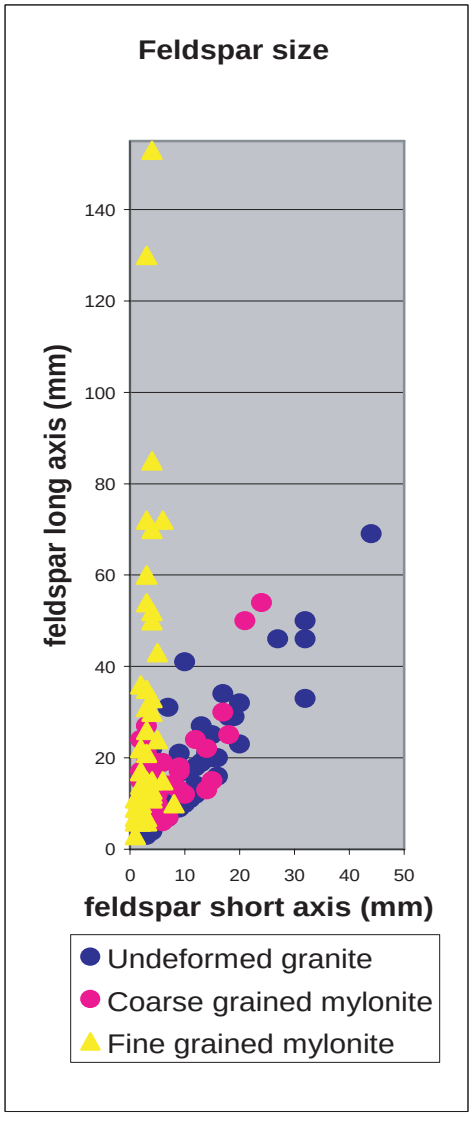

Figure 7.

Figure 8.

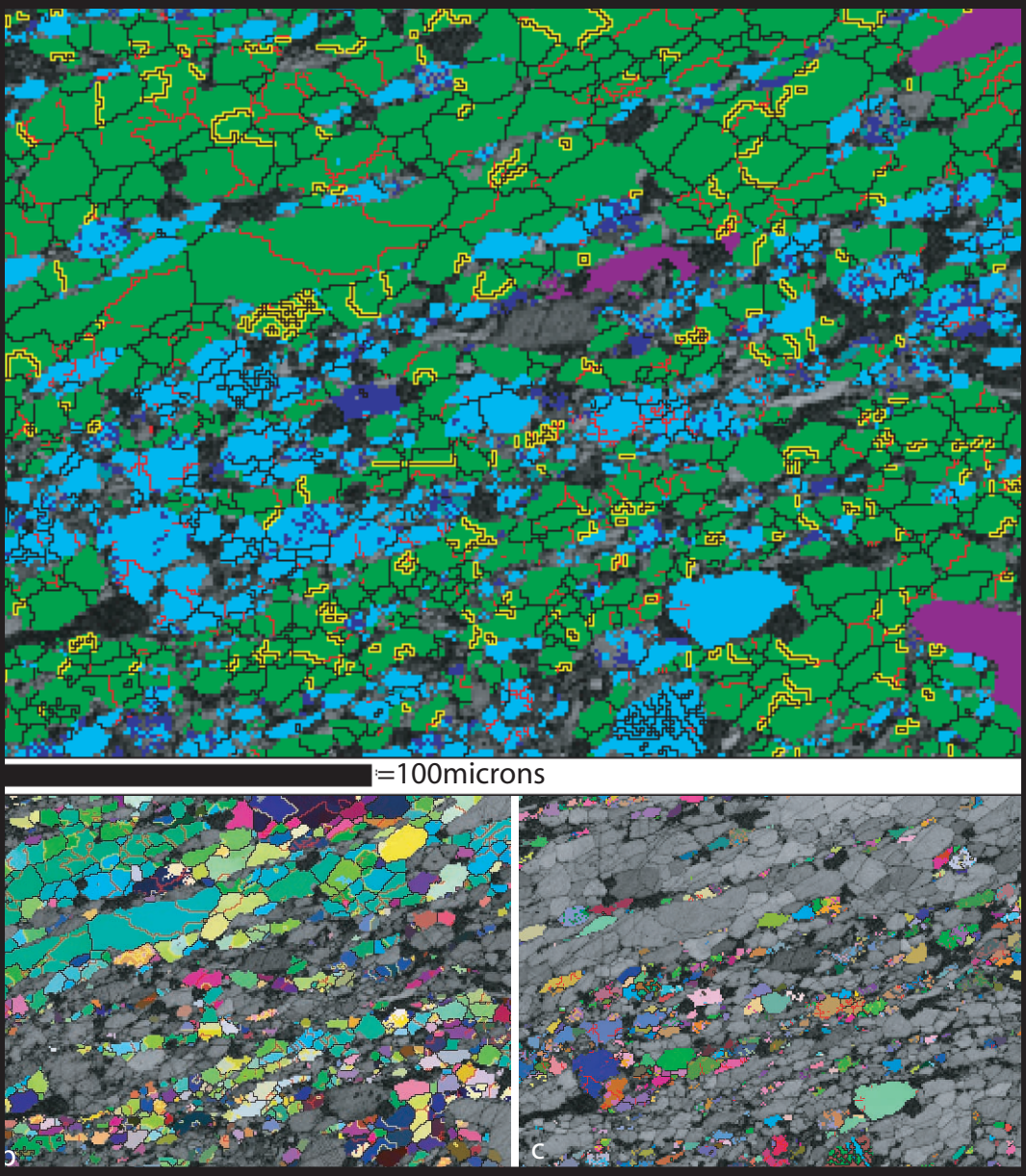

Figure 9.

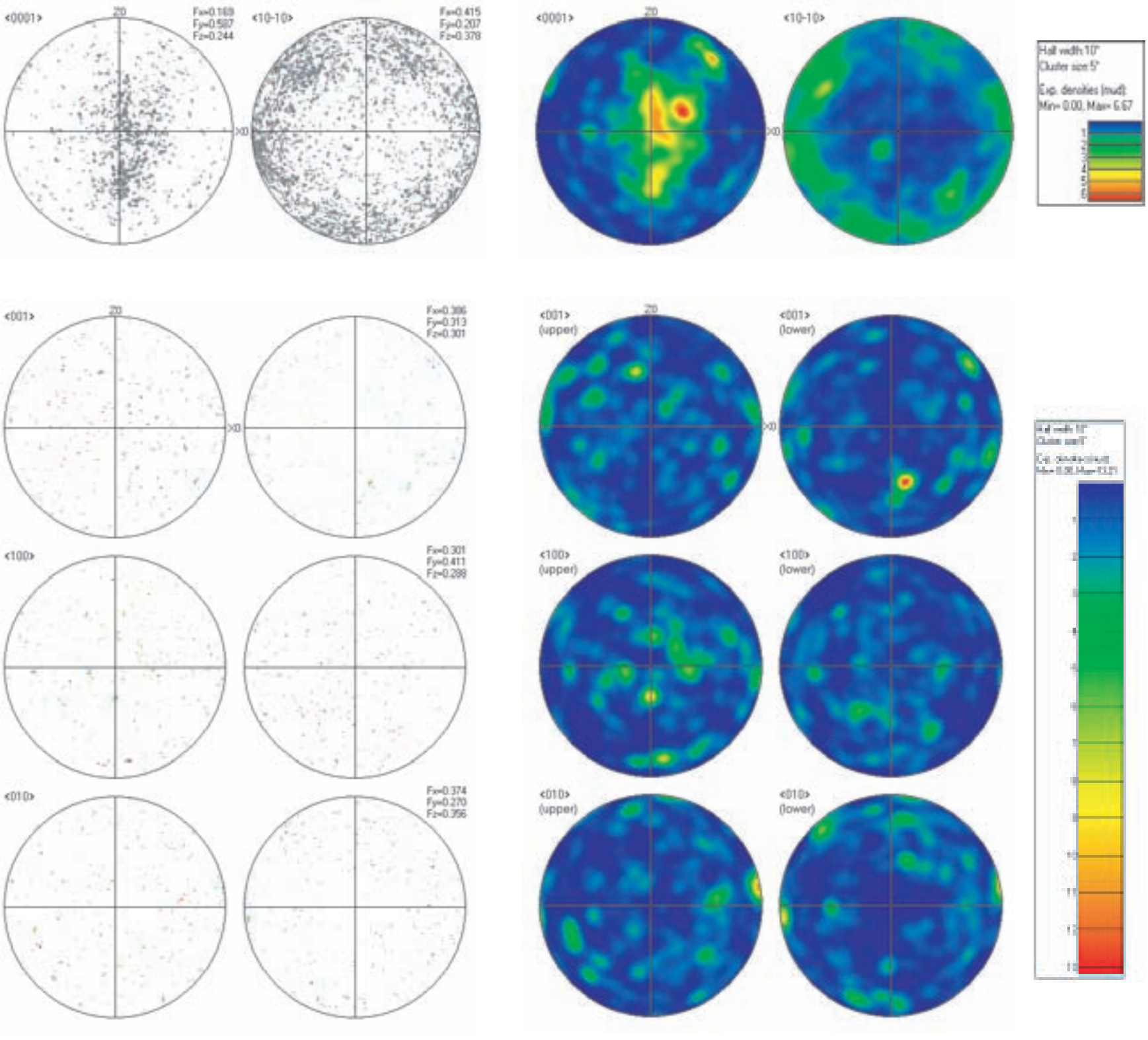

Figure 10. Pole plots and contours for a) quartz c and a axis and b) feldspar, <001>, <010> <100>, using one point per grain subset.

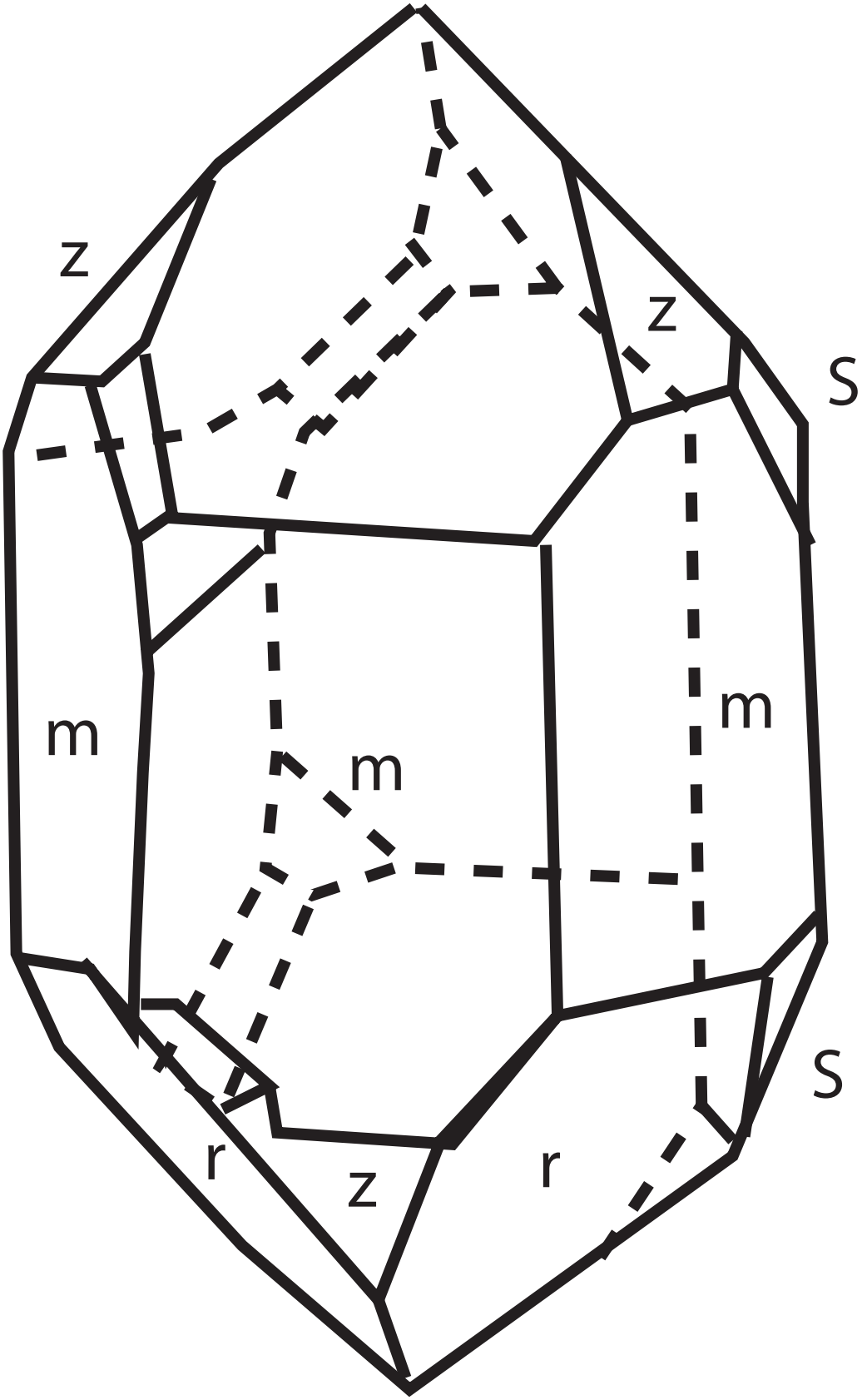

Figure 11. Quartz crystal showing prism (m) and rhomb (r) planes

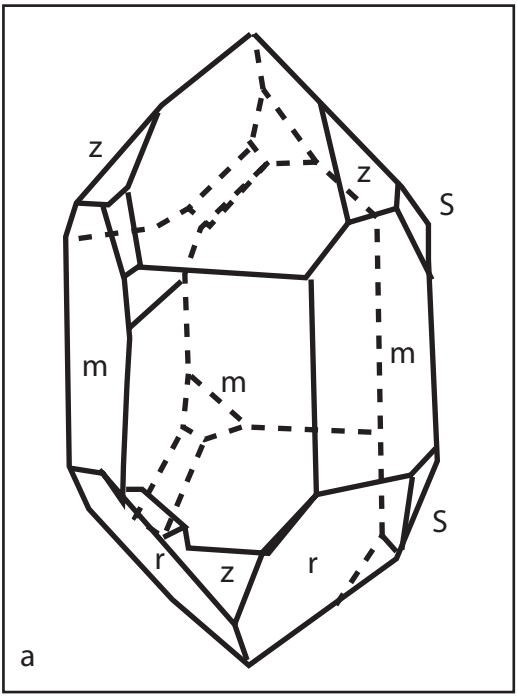

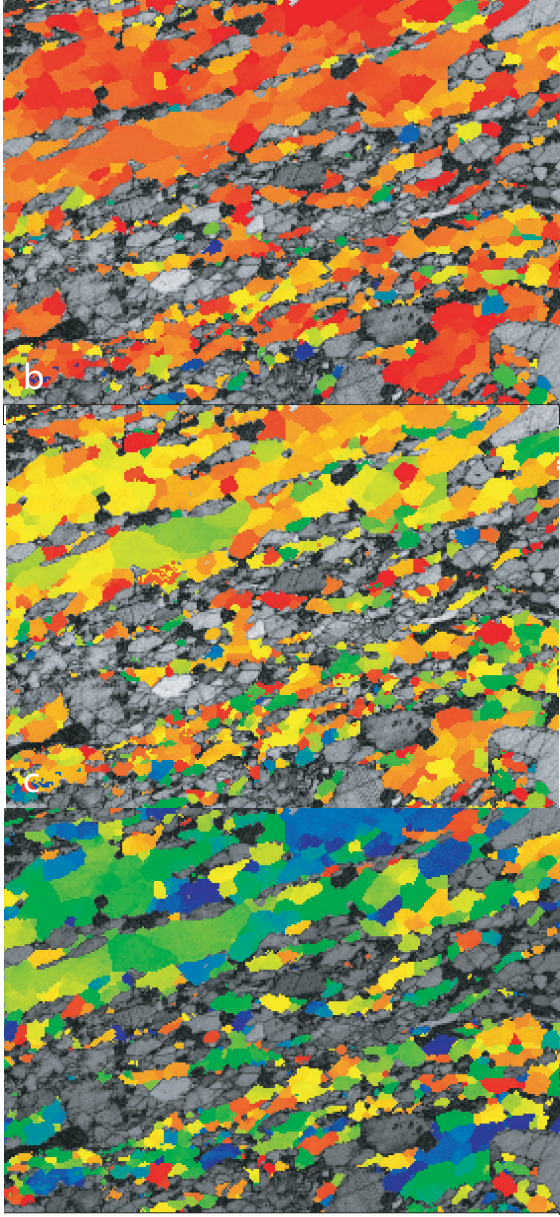

Figure 12.

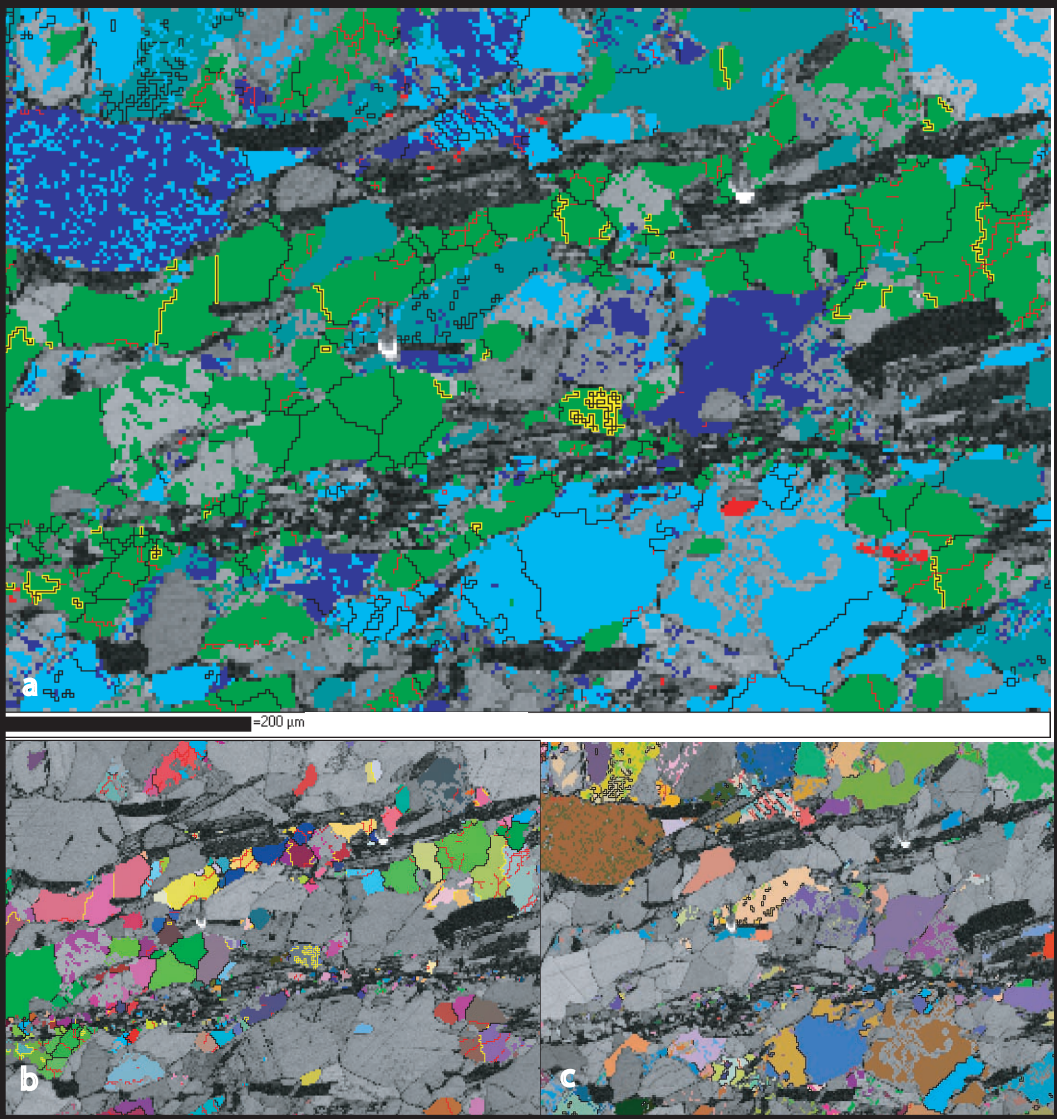

Figure 13.

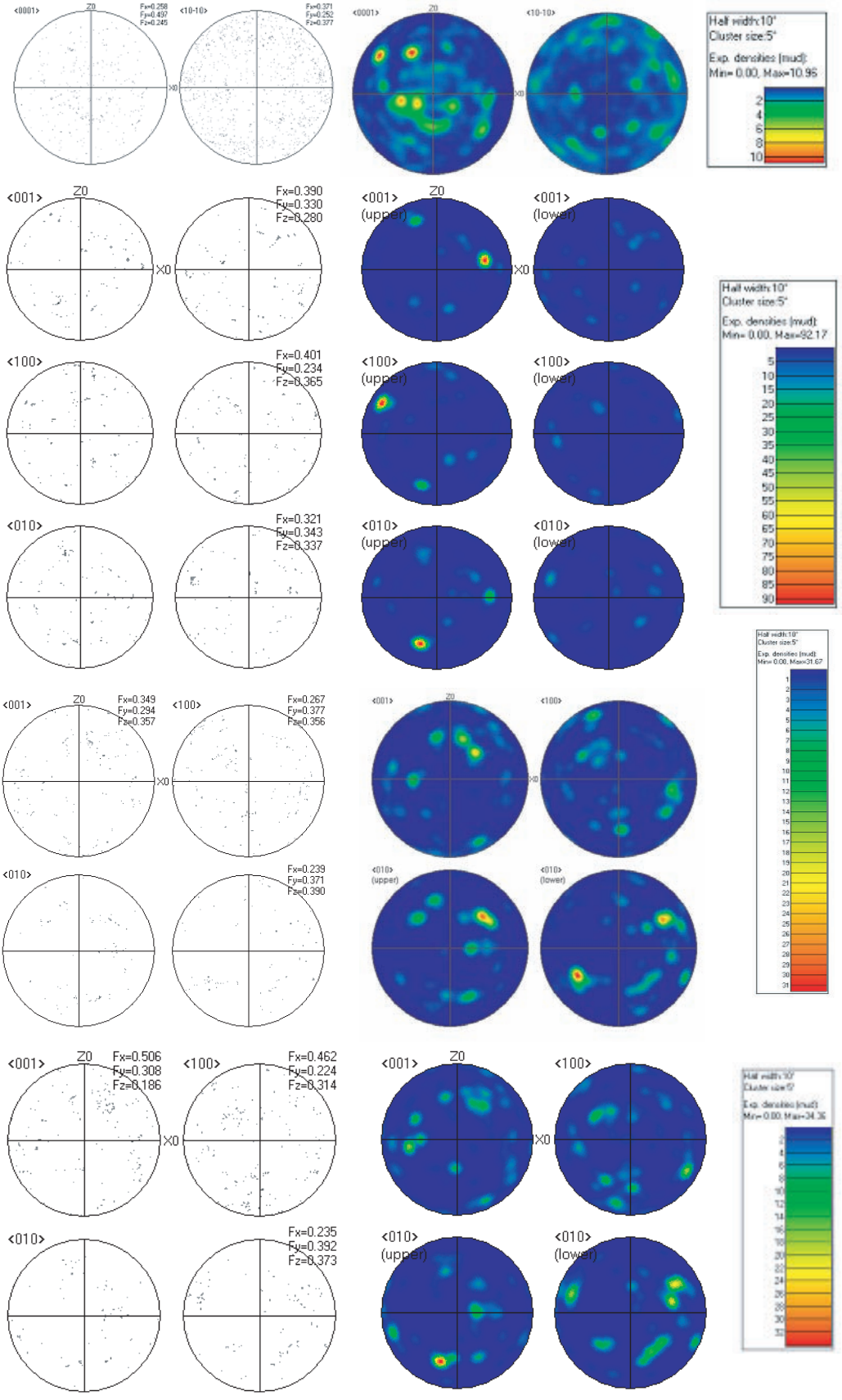
<0001>
Z0
Fx=0.258
Fy=0.497
Fz=0.245
<10-10>
Fx=0.371
Fy=0.252
Fz=0.377
X0
Hall width:10°
Cluster size:5°
Exp. densities (mud):
Min= 0.00, Max=10.96
2
4
6
8
10
<001>
Z0
Fx=0.390
Fy=0.330
Fz=0.280
X0
<001>
(upper)
<001>
(lower)
Hall width:10°
Cluster size:5°
Exp. densities (mud):
Min= 0.00, Max=92.17
5
10
15
20
25
30
35
40
45
50
55
60
65
70
75
80
85
90
<100>
Fx=0.401
Fy=0.234
Fz=0.365
<100>
(upper)
<100>
(lower)
<010>
Fx=0.321
Fy=0.343
Fz=0.337
<010>
(upper)
<010>
(lower)
<001>
Z0
Fx=0.349
Fy=0.294
Fz=0.357
<100>
Fx=0.267
Fy=0.377
Fz=0.356
X0
<010>
Fx=0.239
Fy=0.371
Fz=0.390
Hall width:10°
Cluster size:5°
Exp. densities (mud):
Min= 0.00, Max=31.67
<001>
Z0
<100>
<010>
(upper)
<010>
(lower)
<001>
Z0
Fx=0.506
Fy=0.308
Fz=0.186
<100>
Fx=0.462
Fy=0.224
Fz=0.314
X0
<010>
Fx=0.235
Fy=0.392
Fz=0.373
<001>
Z0
<100>
X0
<010>
(upper)
<010>
(lower)

Figure 15.

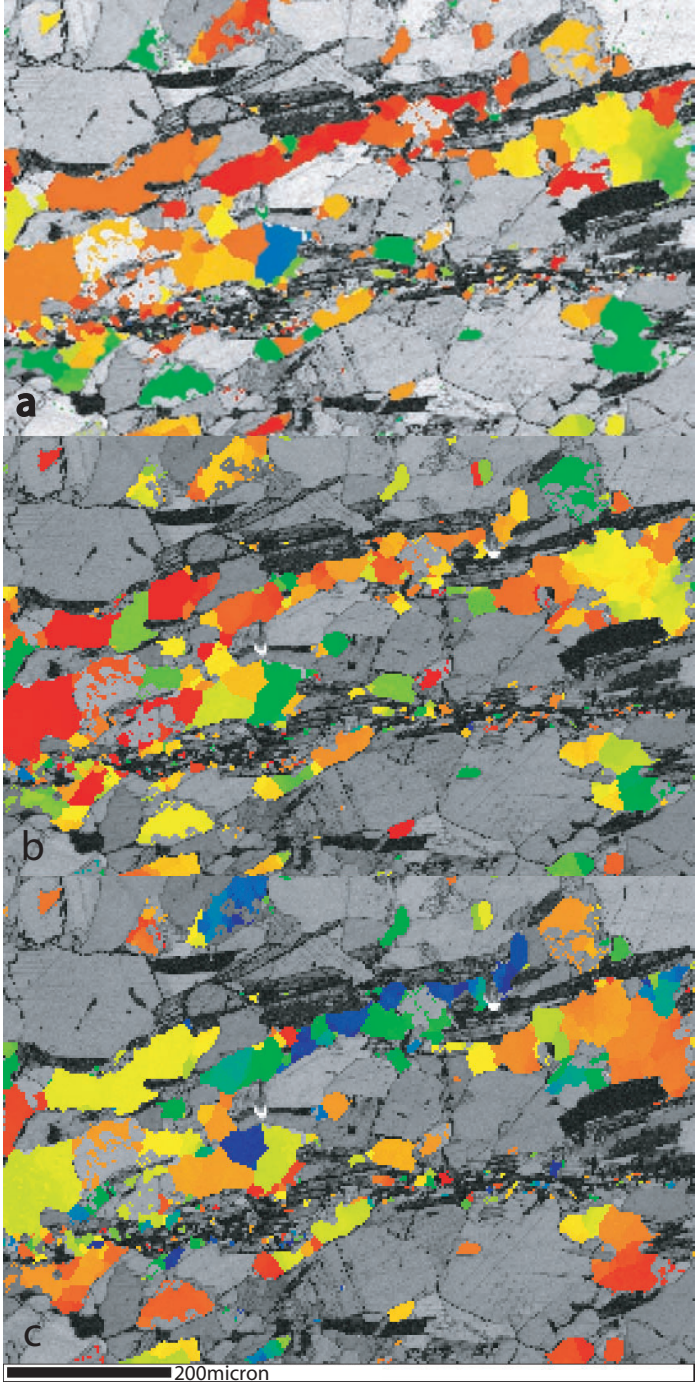

Figure 16.

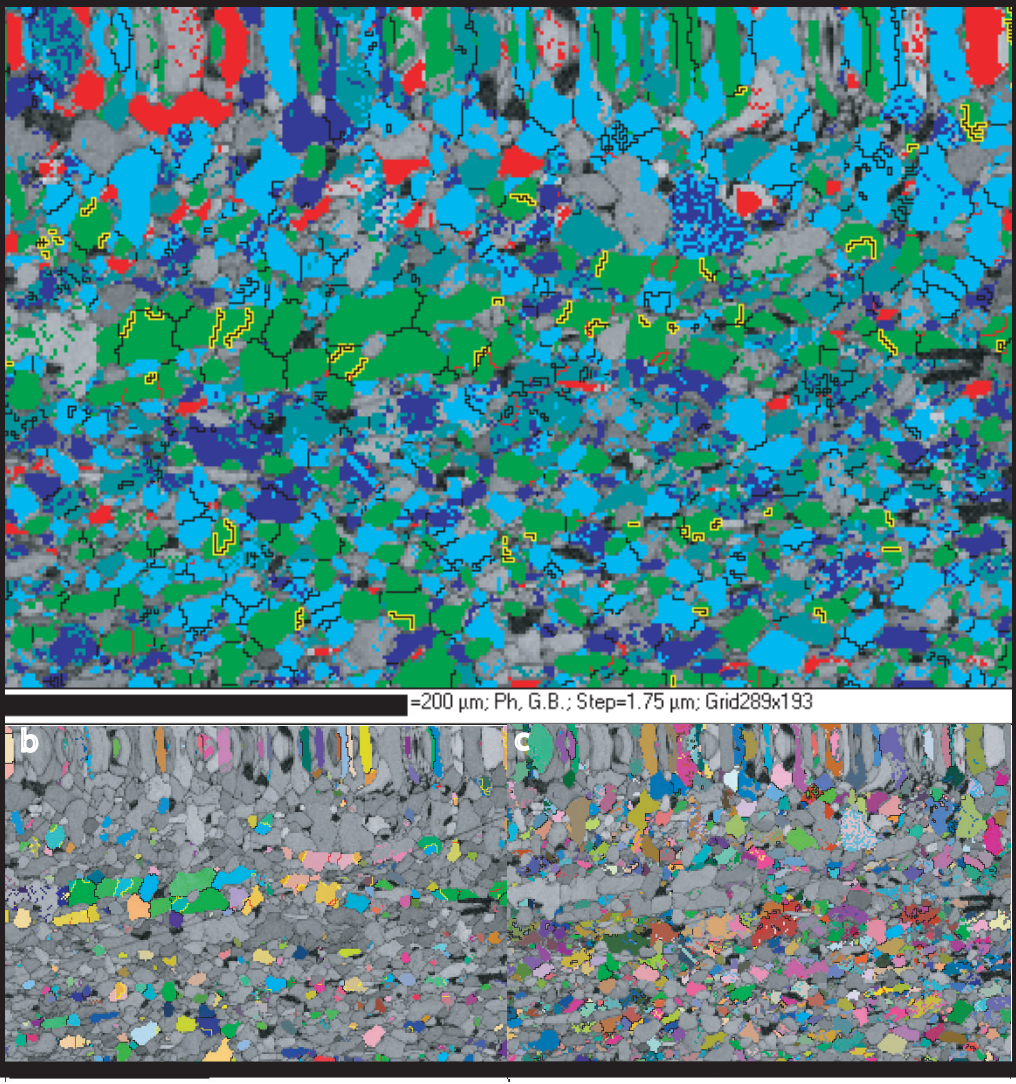

Figure 17.

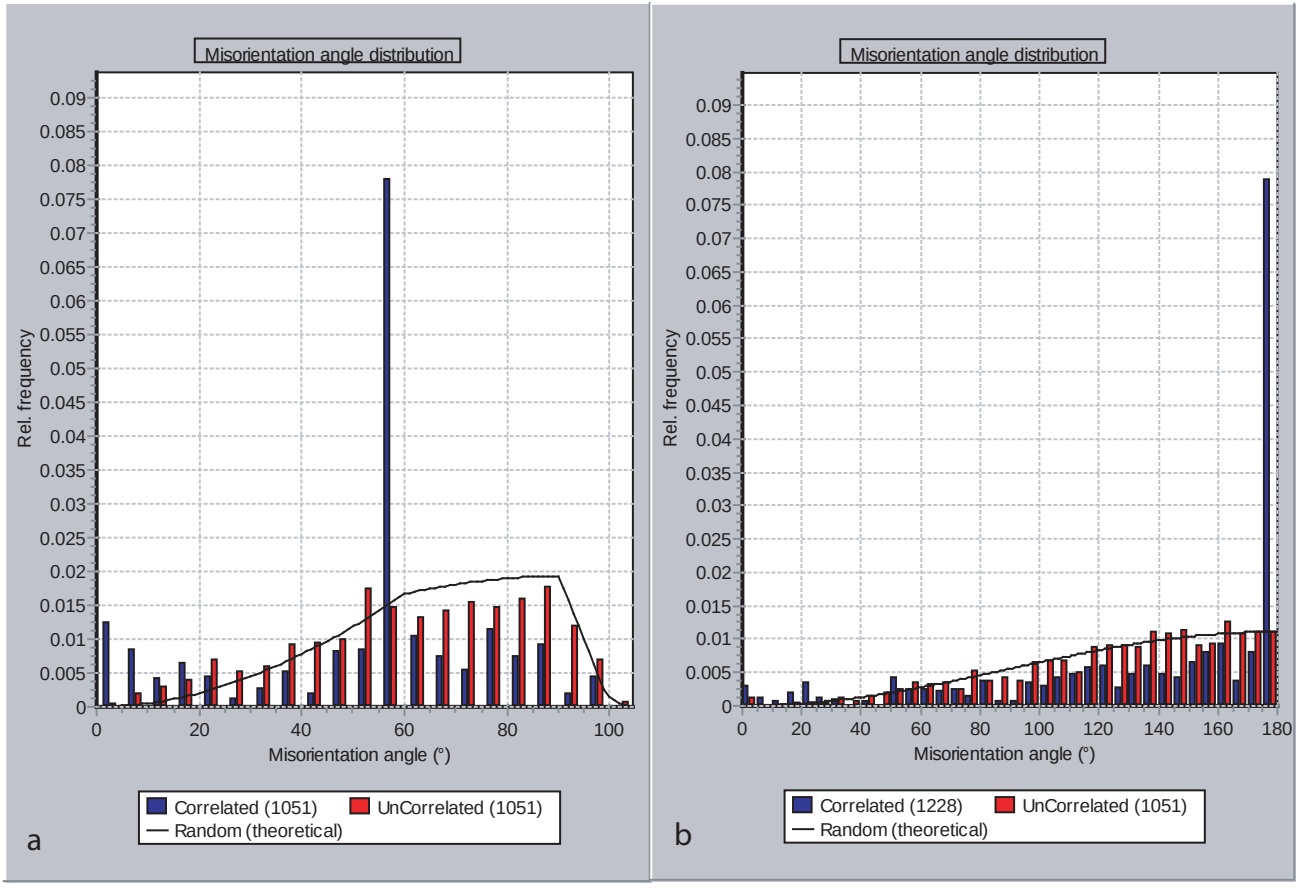
Misorientation angle distribution
Rel. frequency
0.09
0.085
0.08
0.075
0.07
0.065
0.06
0.055
0.05
0.045
0.04
0.035
0.03
0.025
0.02
0.015
0.01
0.005
0
0
20
40
60
80
100
Misorientation angle (°)
Correlated (1051)
UnCorrelated (1051)
Random (theoretical)
a
Misorientation angle distribution
Rel. frequency
0.09
0.085
0.08
0.075
0.07
0.065
0.06
0.055
0.05
0.045
0.04
0.035
0.03
0.025
0.02
0.015
0.01
0.005
0
0
20
40
60
80
100
120
140
160
180
Misorientation angle (°)
Correlated (1228)
UnCorrelated (1051)
Random (theoretical)
b

Figure 18.

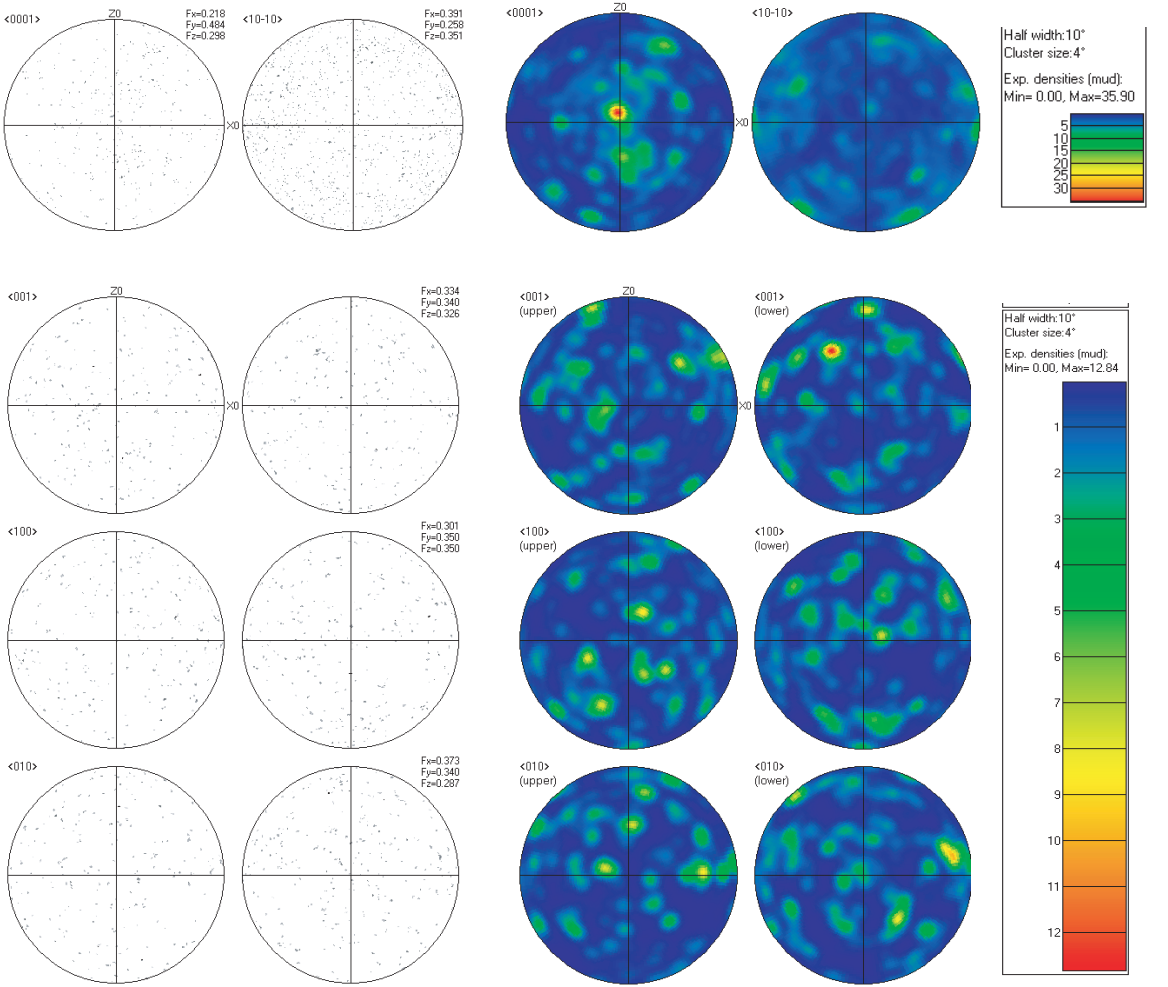
<0001>
Z0
Fx=0.218
Fy=0.484
Fz=0.298
<10-10>
Fx=0.391
Fy=0.258
Fz=0.351
X0
<0001>
Z0
<10-10>
X0
Half width:10°
Cluster size:4°
Exp. densities (mud):
Min= 0.00, Max=35.90
5
10
15
20
25
30
<001>
Z0
Fx=0.334
Fy=0.340
Fz=0.326
X0
<001>
(upper)
Z0
<001>
(lower)
X0
Half width:10°
Cluster size:4°
Exp. densities (mud):
Min= 0.00, Max=12.84
1
2
3
4
5
6
7
8
9
10
11
12
<100>
Fx=0.301
Fy=0.350
Fz=0.350
<100>
(upper)
<100>
(lower)
<010>
Fx=0.373
Fy=0.340
Fz=0.287
<010>
(upper)
<010>
(lower)

Figure 19.

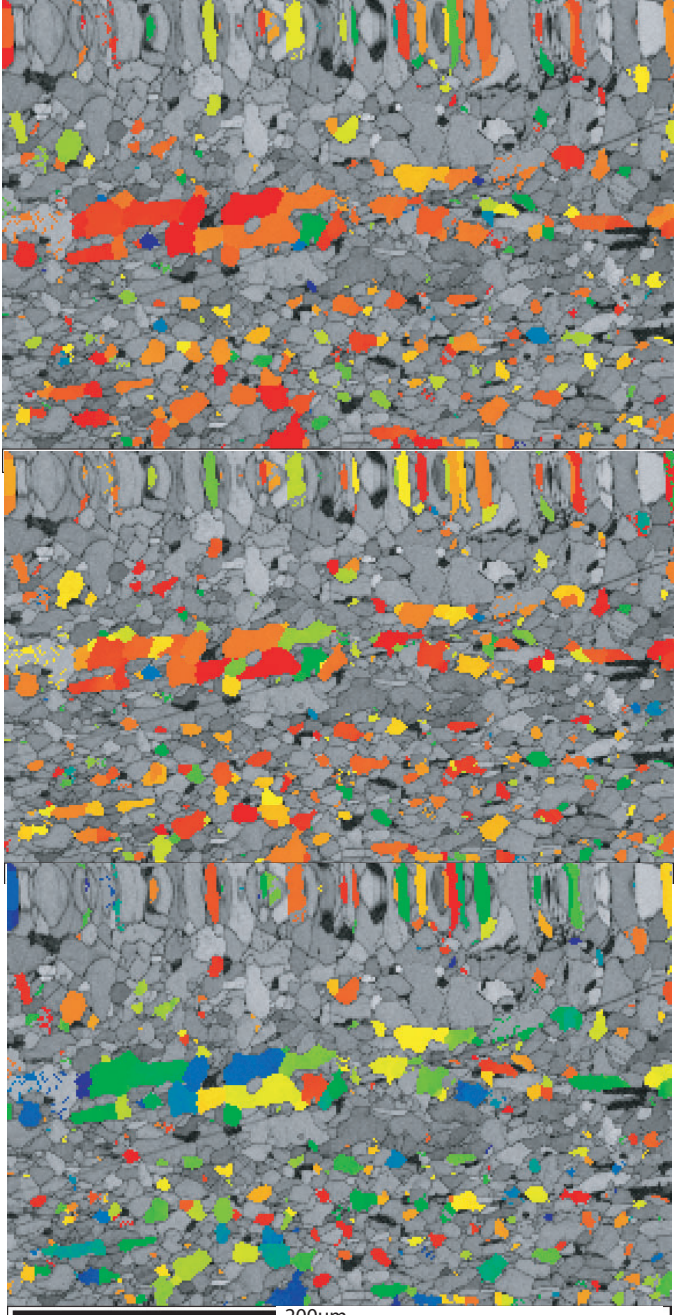

Figure 20.

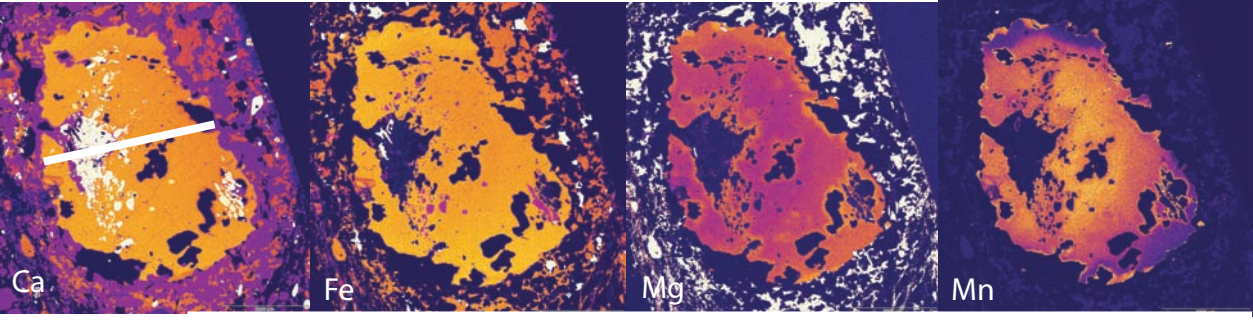

a

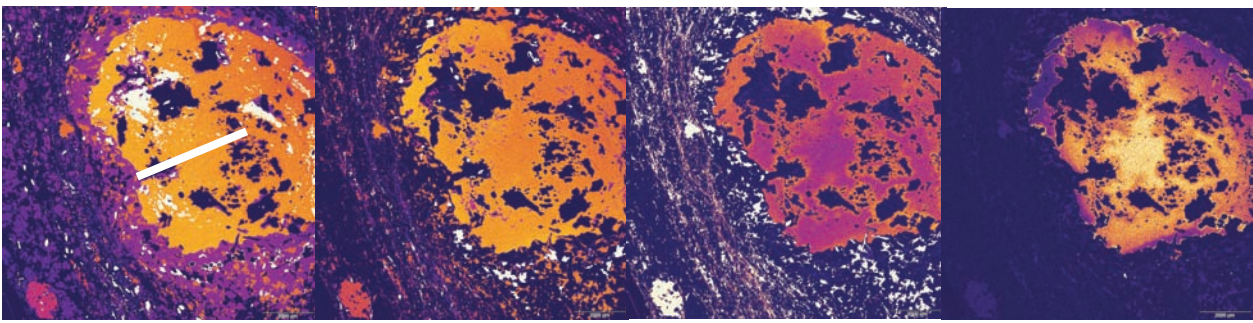

b

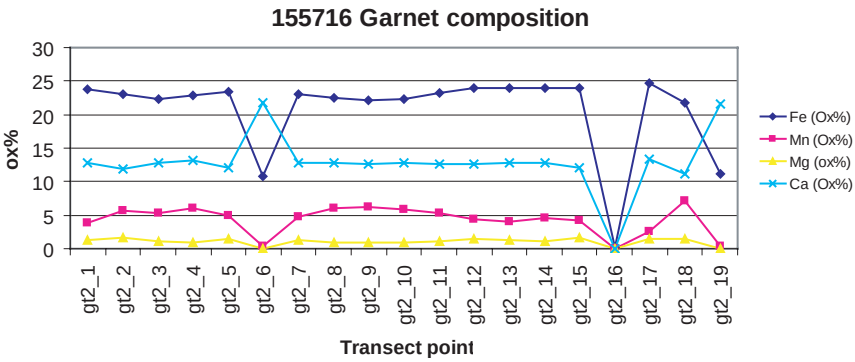

c

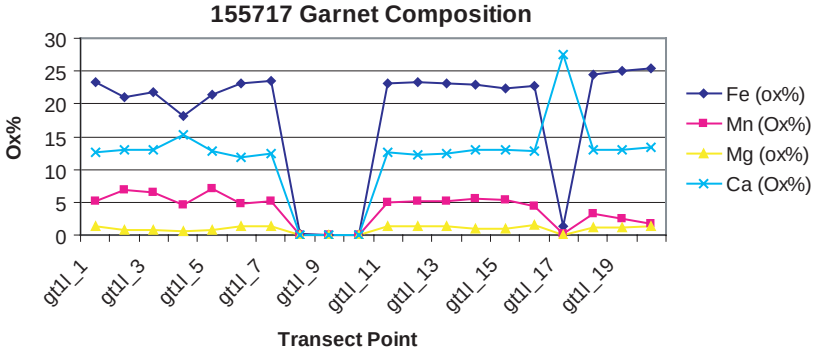

d

Figure 21.

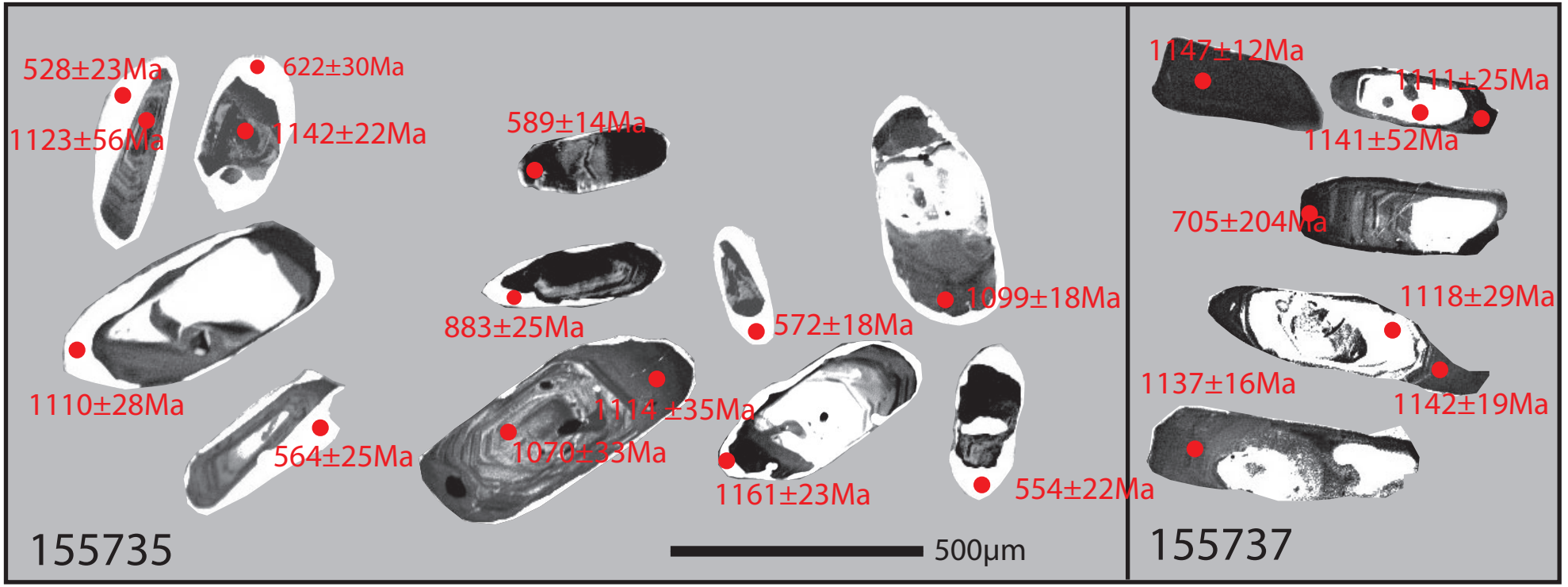
528±23Ma
622±30Ma
1123±56Ma
1142±22Ma
589±14Ma
1099±18Ma
883±25Ma
572±18Ma
1110±28Ma
1114±35Ma
564±25Ma
1070±33Ma
1161±23Ma
554±22Ma
155735
500µm
1147±12Ma
1111±25Ma
1141±52Ma
705±204Ma
1118±29Ma
1137±16Ma
1142±19Ma
155737

Figure 22.

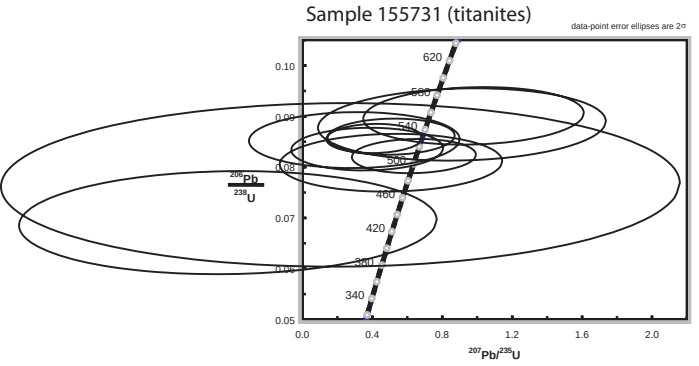
Sample 155731 (titanites)
data-point error ellipses are 2σ
620
560
540
500
460
420
380
340
0.10
0.09
0.08
0.07
0.06
0.05
0.0
0.4
0.8
1.2
1.6
2.0
206Pb/238U
207Pb/235U

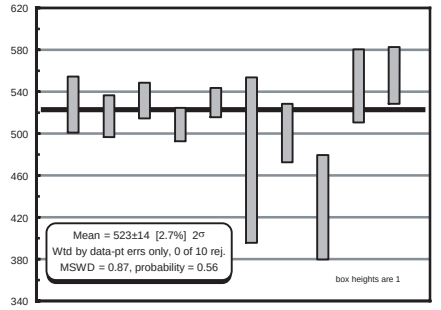
620
580
540
500
460
420
380
340
Mean = 523±14 [2.7%] 2σ
Wtd by data-pt errs only, 0 of 10 rej.
MSWD = 0.87, probability = 0.56
box heights are 1

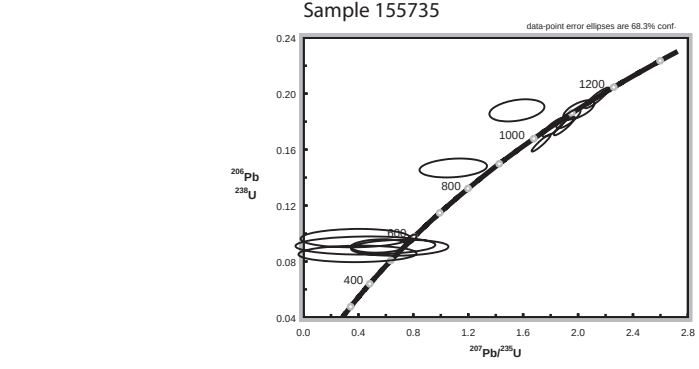
Sample 155735
data-point error ellipses are 68.3% conf.
0.24
0.20
0.16
0.12
0.08
0.04
0.0
0.4
0.8
1.2
1.6
2.0
2.4
2.8
1200
1000
800
600
400
206Pb/238U
207Pb/235U

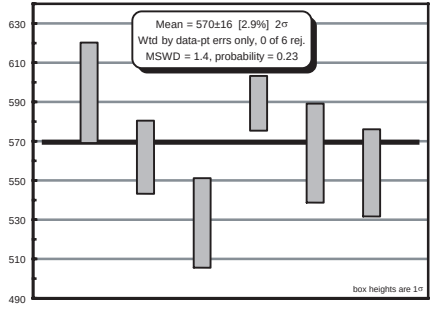
630
610
590
570
550
530
510
490
Mean = 570±16 [2.9%] 2σ
Wtd by data-pt errs only, 0 of 6 rej.
MSWD = 1.4, probability = 0.23
box heights are 1σ

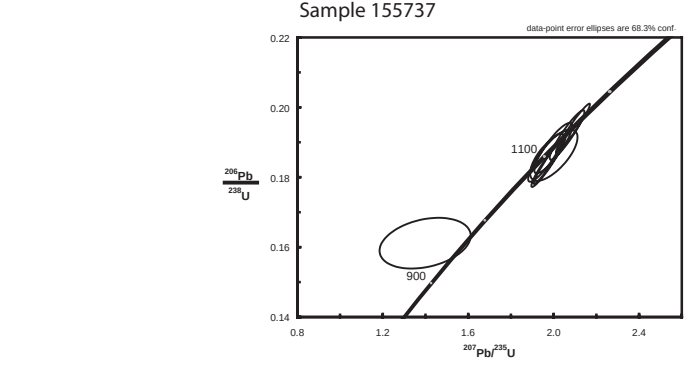
Sample 155737
data-point error ellipses are 68.3% conf.
0.22
0.20
0.18
0.16
0.14
0.8
1.2
1.6
2.0
2.4
1100
900
206Pb/238U
207Pb/235U

Figure 23.

Sample	155716	155718	155732	155737	155717	155730	155735
Min	g	g	g	g	g	g	g
SiO2	36.96	40.86	37.11	38.82	37.7	36.64	38.85
TiO2	0	0.05	0.05	0	0.11	0	0.03
Al2O3	19.65	19.36	20.13	20.54	19.69	19.79	19.23
Cr2O3	0.06	0.03	0	0	0	0	0
Fe2O3	2.68	0	2.71	0	2.26	2.44	0.27
FeO	21.37	25.08	23.11	25.19	21.19	18.46	22.6
MnO	3.81	4.71	3.94	4.73	5.1	9.82	6.67
MgO	1.26	2.06	1.51	1.74	1.38	0.6	1.29
CaO	12.77	8.33	11.31	9.76	12.57	11.16	11.48
Na2O	0.06	0.01	0.03	0.04	0.06	0	0.03
K2O	0.02	0	0	0.03	0	0.01	0
Totals	98.37	100.5	99.62	100.85	99.83	98.68	100.41
Oxygens	12	12	12	12	12	12	12
Si	2.987	3.203	2.968	3.062	3.005	2.978	3.091
Ti	0	0.003	0.003	0	0.007	0	0.002
Al	1.872	1.79	1.899	1.91	1.85	1.897	1.803
Cr	0.004	0.002	0	0	0	0	0
Fe3	0.163	0	0.163	0	0.135	0.149	0.016
Fe2	1.444	1.645	1.546	1.662	1.412	1.254	1.503
Mn	0.261	0.313	0.267	0.316	0.345	0.676	0.45
Mg	0.152	0.241	0.18	0.204	0.164	0.073	0.153
Ca	1.106	0.7	0.97	0.825	1.073	0.972	0.978
Na	0.01	0.002	0.005	0.005	0.009	0	0.004
K	0.002	0	0	0.003	0	0.001	0
Sum	8	7.899	8	7.988	8	8	8
Py	5.12	8.31	6.08	6.80	5.48	2.44	4.96
Alm	48.75	56.75	52.19	55.26	47.17	42.17	48.75
Gro	37.32	24.15	32.72	27.43	35.85	32.66	31.72
Sp	8.80	10.79	9.01	10.51	11.50	22.72	14.57

Sample	155732	155716	155718	155718	155717	155735	155730
Min	fsp	fsp	fsp	fsp	fsp	fsp	fsp
SiO2	62.92	61.29	66.78	65.1	60.8	64.67	61.8
TiO2	0	0.07	0	0	0	0.05	0
Al2O3	22.91	23.94	18.44	22.99	16.46	23.57	22.2
Cr2O3	0.03	0.04	0	0	0	0	0.02
	0.08	0.12	0.46	0.7	0	0.21	0.27
FeO	0	0	0	0	0	0	0
MnO	0	0.02	0	0.01	0.03	0.01	0.04
MgO	0	0	0	0	0.01	0	0.02
CaO	4.69	4.69	0.03	4.6	0.02	5.25	4.68
Na2O	8.64	8.87	0.9	8.71	1.01	8.44	8.54
K2O	0.29	0.21	15.29	0.18	14.8	0.16	0.14
Totals	99.56	99.24	101.92	102.3	93.14	102.36	97.72
Oxygens	8	8	8	8	8	8	8
Si	2.795	2.74	3.012	2.813	3.017	2.793	2.799
Ti	0	0.002	0	0	0	0.002	0
Al	1.2	1.261	0.981	1.171	0.963	1.2	1.185
Cr	0.001	0.001	0	0	0	0	0.001
Fe3	0.003	0.004	0.015	0.023	0	0.007	0.009
Fe2	0	0	0	0	0	0	0
Mn	0	0.001	0	0	0.001	0	0.002
Mg	0	0	0	0	0.001	0	0.001
Ca	0.223	0.224	0.001	0.213	0.001	0.243	0.227
Na	0.744	0.769	0.078	0.73	0.097	0.706	0.75
K	0.017	0.012	0.88	0.01	0.937	0.009	0.008
Sum	4.983	5.015	4.969	4.96	5.018	4.96	4.983
An	22.69	22.34	0.15	22.36	0.10	25.35	23.05
Ab	75.64	76.47	8.20	76.60	9.39	73.73	76.13
Or	1.67	1.19	91.65	1.04	90.51	0.92	0.82

Sample	155718	155732	155716	155737	155717	155730	155735
Min	amph	amph	amph	amph	amph	amph	amph
SiO2	41.32	37.96	38.92	40.66	38.95	38.73	40.9
TiO2	1.28	1.01	1.15	1.15	1.22	0.81	1.18
Al2O3	11.89	12.36	12.87	12.26	12.06	12.73	12.78
Cr2O3	0.01	0.02	0.01	0	0.2	0	0.01
	2.51	4.47	4.94	2.37	3.36	4.68	2.52
FeO	17.61	20.02	17.11	19.7	18.01	19.63	20.23
MnO	0.27	0.58	0.66	0.43	0.69	0.59	0.52
MgO	7.85	5.24	6.96	6.19	6.87	5.36	5.96
CaO	10.63	10.58	10.65	10.38	10.59	10.85	10.61
Na2O	1.47	1.6	1.61	1.56	1.66	1.35	1.59
K2O	1.97	2.06	1.87	2.04	1.96	1.99	1.94
Totals	96.57	95.46	96.28	96.51	95.22	96.26	97.98
Oxygens	23	23	23	23	23	23	23
Si	6.371	6.08	6.076	6.344	6.171	6.119	6.296
Ti	0.148	0.121	0.135	0.134	0.145	0.096	0.137
Al	2.162	2.333	2.369	2.256	2.252	2.37	2.319
Cr	0.001	0.002	0.002	0	0.025	0	0.001
Fe3	0.292	0.539	0.58	0.279	0.401	0.557	0.293
Fe2	2.27	2.68	2.234	2.571	2.386	2.593	2.604
Mn	0.036	0.079	0.088	0.057	0.092	0.079	0.068
Mg	1.804	1.251	1.619	1.44	1.622	1.262	1.367
Ca	1.756	1.816	1.781	1.735	1.798	1.837	1.75
Na	0.44	0.498	0.486	0.473	0.509	0.415	0.473
K	0.388	0.422	0.373	0.406	0.395	0.402	0.382
Sum	15.768	16.009	15.945	15.79	15.937	15.923	15.789
Mg/(Mg+Fe)	0.44	0.32	0.42	0.36	0.40	0.33	0.34

Sample	155718	155716	155732	155737	155737	155730	155735	155717
Min	sp	sp	sp	sp	ilhem	sp	sp	sp
SiO2	0.02	0.02	0.02	0.18	0.06	0.06	0.23	0.08
TiO2	0.33	12.74	0.01	0.04	47.87	0.04	0.45	0
Al2O3	0.19	0.09	0.23	0.12	0	0.12	0.34	0.13
Cr2O3	0	0.05	0	0	0	0	0.04	0
	67.43	40.74	68.45	67.07	4.86	69.58	64.14	67.07
FeO	30.91	41.04	30.92	30.6	40.23	31.48	29.98	30.2
MnO	0.02	0.04	0.1	0.08	2.31	0.12	0.08	0.15
MgO	0.01	0.05	0	0.02	0.27	0	0.02	0.03
CaO	0	0.04	0	0.04	0.06	0	0.21	0.02
Na2O	0.01	0.03	0	0	0	0	0	0
K2O	0.02	0	0	0	0	0	0.03	0.01
Totals	92.19	90.76	92.88	91.44	95.18	94.43	89.08	90.96
Oxygens	4	4	4	4	3	4	4	4
Si	0.001	0.001	0.001	0.007	0.002	0.002	0.009	0.003
Ti	0.01	0.383	0	0.001	0.95	0.001	0.014	0
Al	0.009	0.004	0.011	0.006	0	0.005	0.016	0.006
Cr	0	0.002	0	0	0	0	0.001	0
Fe3	1.972	1.227	1.987	1.978	0.097	1.988	1.939	1.988
Fe2	1.005	1.374	0.998	1.003	0.888	1	1.007	0.995
Mn	0.001	0.001	0.003	0.003	0.052	0.004	0.003	0.005
Mg	0.001	0.003	0	0.001	0.01	0	0.001	0.002
Ca	0	0.002	0	0.002	0.002	0	0.009	0.001
Na	0.001	0.002	0	0	0	0	0	0
K	0.001	0	0	0	0	0	0.001	0
Sum	3	3	3	3	2	3	3	3

Sample	155730	155718	155716	155732	155737	155717	155735
Min	bi	bi	bi	bi	bi	bi	bi
SiO2	35.45	49.47	35.24	35.81	35.98	35.03	37.22
TiO2	2.37	2.45	2.41	2.93	3.61	1.87	2.33
Al2O3	14.31	18.47	15.38	13.76	13.93	14.8	14.91
Cr2O3	0.01	0	0	0	0.01	0	0
	0	0	1.8	0	0	0.31	0
FeO	23.89	11.61	19.04	24.3	22.69	21.88	23.06
MnO	0.43	0.09	0.47	0.4	0.29	0.41	0.5
MgO	7.98	7.09	10.59	8.17	8.57	8.95	8.41
CaO	0.04	2.01	0.08	0	0.08	0.14	0.28
Na2O	0.08	3.87	0.05	0.1	0.13	0.11	0.08
K2O	8.68	5.65	9.01	9.33	9.44	8.8	8.99
Totals	93.26	100.7	93.89	94.8	94.74	92.27	95.8
Oxygens	11	11	11	11	11	11	11
Si	2.832	3.296	2.743	2.829	2.822	2.808	2.87
Ti	0.142	0.123	0.141	0.174	0.213	0.112	0.135
Al	1.348	1.451	1.411	1.281	1.288	1.398	1.355
Cr	0.001	0	0	0	0.001	0	0
Fe3	0	0	0.106	0	0	0.019	0
Fe2	1.596	0.647	1.239	1.606	1.488	1.465	1.487
Mn	0.029	0.005	0.031	0.027	0.019	0.028	0.033
Mg	0.951	0.703	1.229	0.962	1.001	1.069	0.966
Ca	0.003	0.143	0.006	0	0.006	0.012	0.023
Na	0.013	0.499	0.007	0.015	0.02	0.017	0.012
K	0.885	0.48	0.895	0.94	0.945	0.9	0.885
Sum	7.801	7.347	7.809	7.834	7.804	7.83	7.766
Fe/(Fe+Mg)	0.63	0.48	0.50	0.63	0.60	0.58	0.61

Table 1. Summary of Mineral CHemistry for Spaghetti Hill shear zones. g=garnet, amph=amphibole, sp=spinel, ilhem = ilmenite, bi= biotite.

Independent set of reactions

1) 2gr + 7phl + 24q = 2py + 3tr + 4H2O + 7san
2) 6an + 11phl + 30q = 6py + 3tr + 8H2O + 11san
3) py + ann = alm + phl
4) 3parg + 4phl + 24q = 3py + 3ab + 3tr + 4H2O + 4san
5) 6gr + 6an + 6ab + 3gl + 13phl = 12parg + 4H2O + 13san
6) 16alm + 15phl + 24sph = 10py + 6gr + 3tr + 24usp + 12H2O + 15san
7) 3gr + 3mt + 2phl + 9q = 2py + alm + 3andr + 2H2O + 2san

Sample	**AvT (ºC)**	sd	2σ	**AvP (Kbars)**	sd	2σ	cor	sigfit	excluded
155716	644	149	298	11.7	2.5	5.0	0.849	1.33	water and usp
155717	589	110	220	9.6	1.9	3.8	0.828	1.20	water
155718	669	131	262	6.0	1.9	3.8	0.709	1.06	water and east
155730	793	217	434	11.5	1.6	3.2	0.863	1.30	water
155732	788	324	648	11.8	6.0	12.0	0.876	1.74	water and parg
155735	734	148	296	10.8	2.5	5.0	0.896	0.82	water usp parg
155737	863	187	374	12.6	2.5	5.0	0.859	1.36	water
Average	725.71			10.57					

Table 2. Average P-T estimates, excluding water.

Sample 155716								MSWD:1.45
a H2O	550ºC ± 2σ	fit	600ºC ± 2σ	fit	650ºC ± 2σ	fit	700ºC ± 2σ	fit
0.2	9.8±2.32	1.4	10.1±2.96	1.6	10.5±3.76	2	10.8±4.64	2.3
0.4	10.3±1.96	1.2	10.7±2.18	1.2	11.0±2.70	1.4	11.4±3.40	1.7
0.6	10.6±2.10	1.2	11.0±2.0	1.1	11.4±2.28	1.4	11.8±2.8	1.4
0.8	10.9±2.34	1.4	11.2±2.06	1.1	11.6±2.12	1.1	12.0±2.48	1.2

Table 3. Average pressure (Kbars) at temperature (ºC) demonstrating the estimate variability with increasing water activity.

Av PT with most likely water activity								
	aH20	AvT	Sd	Av P	Sd	Corr	Sd	Sigfit
155716	0.8	705	71	10.8	1.6	0.578	1.57	fits
155717	0.9	560	42	9.1	0.9	0.285	1.12	fits
155718	0.2	642	90	7.3	1.9	0.415	1.7	fits
155730	1.0	637	58	10.6	1.4	0.488	0.54	fits
155732	1.0	622	99	9.2	1.8	-0.093	1.9	fits
155735	1.0	593	86	8.8	1.9	0.305	2.17	does not fit
155737	1.0	749	184	9.8	2.9	0.38	3.48	does not fit

Table 4. Average Pressure-Temperature estimateswith the water activity that most closely resembles the dry estimate.

Zircon Analyses

	U	Th		206Pb	204Pb/		Radiogenic Ratios							Apparent age (Ma)		
Labels	ppm	ppm	Th/U	ppm	206Pb	206f%	206Pb/238U	±	207Pb/235U	±	207Pb/206Pb	±	rho	206Pb/238U	±	207Pb/206Pb
735-1.1	173.599	105.955	0.631	27.27	16.86475	0.42	0.1821	2.5	1.9263	3.0	0.0767	1.8	0.82	1078	24	1114
735-1.2	102.538	79.950	0.806	15.53	16.94487	0.18	0.1760	2.5	1.8211	3.0	0.0750	1.7	0.84	1045	24	1070
735-2.1	11.659	0.789	0.070	1.03	18.7033	5.92	0.0967	4.5	0.3793	69.1	0.0285	68.9	0.07	595	26	-1323
735-2.2	230.500	250.932	1.125	35.00	16.81514	-0.01	0.1767	2.4	1.8964	2.7	0.0778	1.1	0.91	1049	24	1142
735-3.1	26.252	0.163	0.006	2.12	18.7033	2.96	0.0911	3.5	0.5547	24.4	0.0442	24.1	0.14	562	19	-101
735-4.1	20.240	2.867	0.146	1.68	18.7033	11.80	0.0854	4.5	0.3956	71.6	0.0336	71.4	0.06	529	23	-825
735-4.2	226.112	244.346	1.117	36.92	16.84846	0.89	0.1883	2.5	2.0018	3.7	0.0771	2.8	0.66	1112	25	1123
735-5.1	269.433	172.544	0.662	38.12	16.89267	0.00	0.1647	2.4	1.7293	2.6	0.0762	0.9	0.94	983	22	1099
735-6.1	250.044	137.970	0.570	20.61	17.7886	0.22	0.0957	2.5	0.7828	3.5	0.0593	2.5	0.71	589	14	578
735-7.1	234.023	144.793	0.639	39.60	16.78041	0.06	0.1968	2.5	2.1325	2.7	0.0786	1.1	0.91	1158	26	1161
735-8.1	33.714	11.863	0.364	4.38	18.12156	2.92	0.1468	3.0	1.0914	14.8	0.0539	14.4	0.21	883	25	368
735-9.1	47.049	23.798	0.523	7.77	17.74629	2.21	0.1879	2.8	1.5527	8.5	0.0599	8.0	0.32	1110	28	601
735-10.1	18.509	1.605	0.090	1.56	18.7033	7.06	0.0914	4.7	0.4529	74.2	0.0359	74.0	0.06	564	25	-637
735-11.1	16.079	0.613	0.039	1.25	17.94763	0.83	0.0897	4.2	0.7016	33.3	0.0567	33.1	0.13	554	22	480
737-1.1	89.579	66.270	0.764	14.42	16.81666	0.53	0.1864	2.6	1.9986	3.7	0.0778	2.6	0.70	1102	26	1141
737-1.2	228.941	144.554	0.652	36.58	16.87061	0.14	0.1857	2.4	1.9620	2.8	0.0766	1.3	0.89	1098	25	1111
737-2.1	36.748	37.844	1.064	5.19	17.57281	1.86	0.1613	3.0	1.3990	10.0	0.0629	9.6	0.30	964	27	705
737-2.2	371.324	246.886	0.687	58.99	16.82279	0.01	0.1849	2.4	1.9797	2.5	0.0777	0.6	0.97	1094	24	1138
737-3.1	272.560	169.792	0.644	45.05	16.81508	0.12	0.1922	2.4	2.0619	2.6	0.0778	0.9	0.93	1133	25	1142
737-3.2	101.145	84.633	0.865	16.39	16.85897	0.10	0.1884	2.5	1.9971	2.9	0.0769	1.4	0.87	1113	26	1118
737-4.1	322.233	226.063	0.725	50.98	16.82439	0.08	0.1840	2.4	1.9693	2.5	0.0776	0.8	0.95	1089	24	1137
737-5.1	478.625	391.281	0.845	79.84	16.8063	0.02	0.1941	2.4	2.0882	2.5	0.0780	0.6	0.97	1144	25	1147
titanites						4f206							%conc			
731-1.1	29	5	0.189	7	0.021	0.372	0.085	0.005	0.294	0.495	0.025	0.042	22	822	18	3667
731-2.1	37	6	0.162	7	0.016	0.292	0.084	0.003	0.372	0.355	0.032	0.031	21	719	15	3350
731-3.1	41	10	0.253	8	0.014	0.256	0.086	0.003	0.509	0.295	0.043	0.025	22	706	13	3221
731-4.1	53	9	0.176	10	0.015	0.265	0.082	0.003	0.639	0.289	0.056	0.025	21	683	11	3322
731-5.1	54	10	0.177	9	0.012	0.220	0.086	0.002	0.414	0.224	0.035	0.019	23	672	11	2979
731-6.1	12	2	0.182	9	0.041	0.723	0.077	0.013	0.192	1.604	0.018	0.152	34	1572	48	4593
731-7.1	25	5	0.207	7	0.022	0.397	0.081	0.005	0.506	0.519	0.045	0.046	21	811	19	3808
731-8.1	20	6	0.313	10	0.037	0.658	0.069	0.008	-0.448	-0.993	-0.047	0.105	27	1185	30	4403
731-9.1	21	3	0.126	7	0.024	0.434	0.088	0.006	0.912	0.671	0.075	0.054	23	936	23	3987
731-10.1	25	4	0.165	7	0.020	0.359	0.090	0.005	0.979	0.513	0.079	0.041	23	848	19	3768

Table 5. SHRIMP U-Pb zircon and titanite data.

RECORD 2009/14

COMPLEX STRAIN IN MYLONITES FROM THE WESTERN MUSGRAVES, NORTH OF THE MANN FAULT, WESTERN AUSTRALIA

This Record is published in digital format (PDF) and is available online at: www.dmp.wa.gov.au/GSWApublications.
Laser-printed copies can be ordered from the Information Centre for the cost of printing and binding.

Further details of geological publications and maps produced by the Geological Survey of Western Australia can be obtained by contacting:

Information Centre
Department of Mines and Petroleum
100 Plain Street
EAST PERTH, WESTERN AUSTRALIA 6004
Phone: (08) 9222 3459 Fax: (08) 9222 3444
www.dmp.wa.gov.au/GSWApublications

WALKER-HALLAM